Materials Horizons

ROYAL SOCIETY OF CHEMISTRY

REVIEW

View Article Online
View Journal | View Issue

Cite this: *Mater. Horiz.*, 2025, **12**, 8989

Metal–organic frameworks as potential materials for X-ray detectors: recent progress and unique opportunities

Hayden Salway, †[ab] Xian Wei Chua †[ab] and Miguel Anaya *[ac]

Received 22nd August 2024,
Accepted 4th July 2025

DOI: 10.1039/d4mh01122h

rsc.li/materials-horizons

X-ray detectors and scintillators play a crucial role in society, with extensive applications in scientific research, security, manufacturing quality control, and medical imaging, including general radiography, computed tomography, and positron emission tomography. With aging populations globally, the demand for medical imaging is steadily growing, necessitating accessible and affordable X-ray technologies that can provide higher image quality with minimal radiation dosage. Existing commercial technologies possess several drawbacks, including slow response times, poor radioluminescence efficiencies, limited tunability range of X-ray energies, and reliance on costly and energy-intensive production processes. Metal–organic frameworks (MOFs) have recently attracted attention as promising materials for a new generation of X-ray detectors and scintillators that can revolutionise low-dose and high-throughput medical and security imaging and enable unique applications. In this work, we discuss the underlying mechanisms and recent progress made in MOF-based X-ray detectors and scintillators, and examine their unique potential to outperform existing technologies.

Wider impact

This review delves into the advancements of metal organic framework X-ray detectors, exploring their fundamental mechanisms, current performance metrics, and highlighting the unique opportunities MOFs provide to surpass the limitations of existing technologies and create new applications. Future research endeavours in the wider scientific community will persist in pushing the boundaries of sensitivity, leading to improved image clarity and decreased radiation exposure for patients, with MOF's chemical versatility providing substantial promise for developing the next generation of X-ray detectors. In this work, we first provide an overview of current state-of-the-art MOF X-ray detector performances in terms of key figures of merit. Furthermore, we discuss methods used to enhance performance in MOF detectors and their scalability into full-imaging arrays. The review then expands on the unique multi-functionality of MOFs which promises utility in various fields, including bioimaging, drug delivery and radioactive gas detection, alongside classical applications in medical and security imaging. The advancement of economical manufacturing methods and morphological adaptability of MOFs will also play a crucial role in meeting the increasing demand for imaging, making vital healthcare and security X-ray technologies more accessible to society.

1. Introduction

The ability to detect X-rays has had profound importance to society since their discovery in 1885,[1] with vast applications including security, quality control, scientific research, and most significantly in medical imaging such as radiography, positron emission tomography (PET) and computed tomography (CT).[2] As radiation travels through the body, the attenuation varies depending on the tissue, resulting in contrast on the detector and an image providing invaluable insights of what is occurring within the body. Although critical to modern healthcare, X-rays are ionising radiation and pose substantial health risks, with healthcare professionals having to carefully weigh the risks against medical need. Weighing up these decisions is becoming increasingly difficult for clinicians with an ever-increasing demand for routine diagnostic scans, such as CT scans which have increased by a staggering 50% in the UK between 2014 and 2019.[3] This increase is expected to accelerate due to ageing populations in many countries, and national plans for significant increases in routine scans for diseases such as cancer. Apart from their importance in medical imaging, recent applications of X-ray detection include single photon detection for research and multi-spectra imaging.

[a] *Department of Chemical Engineering and Biotechnology, University of Cambridge, Philippa Fawcett Drive, Cambridge CB3 0AS, UK*
[b] *Cavendish Laboratory, Department of Physics, University of Cambridge, JJ Thomson Avenue, Cambridge CB3 0HE, UK*
[c] *Institute of Materials Science of Seville, University of Seville - Spanish National Research Council (US-CSIC), Calle Americo Vespucio 49, Sevilla 41092, Spain. E-mail: anaya@us.es*
† These authors contributed equally.

There are two main classes of radiation detection, named indirect and direct detection, which vary in their method of electrical signal production. Indirect detection proceeds by using a scintillator to down-convert incident X-ray photons to UV-VIS photons, whereas direct detection directly converts X-ray photons into current. Indirect detection is currently the more common commercial technique due to complications in limiting dark current. Current state-of-the-art scintillators such as CsI:Tl, NaI:Tl, $Bi_4Ge_3O_{12}$ (BGO), $(Lu,Y)_2SiO_5$ (LYSO) and Gd_2O_2S:Tb (GOS:Tb) have been commercially successful due to their acceptable light-yields, densities, and decay times. However, these materials have inherent limitations which hinder expansion and development to new uses. For instance, both CsI:Tl and GOS:Tb have a fixed band gap energy (photon emission energy) that cannot be tuned, and to achieve adequate X-ray absorption, they require a large material thickness (5 mm for CsI:Tl), which necessitates expensive high-energy and high-temperature fabrication methods and often complex microstructures are required for wave guiding to improve image resolution.[4–6] Current direct detectors also have inherent limitations: HgI_2 and PbI_2 detectors have large leakage currents; Si and a-Se due to their low atomic number (Z) have low X-ray stopping power, and CdZnTe (CZT), alongside complex energy-intensive synthesis requirements, usually has non-uniform charge transport and large noise levels due to charge trapping.[7,8] Therefore, there is a significant need for the development of new materials for radiation detection.

Metal–organic frameworks (MOFs) are one set of materials which have recently gained research attention as promising materials for new generation X-ray scintillators and direct detectors. MOFs are a class of materials defined by IUPAC as a coordination polymer (or network) with an open framework containing potential voids.[9] A MOF coordination network is formed by metals or metal clusters connected *via* organic linkers. Due to the possible combinations of metals and linkers, there are near infinite theoretical possibilities for MOF designs. Currently, there are over 100 000 synthesised MOFs in the Cambridge Structural Database (CSD), demonstrating the vast versatility and tunability of MOFs towards tailored X-ray applications.[10–12] Alongside their tunability, MOFs' properties such as high porosity, thermal and radiation stabilities, allowing post-synthetic modification and the encapsulation of guest molecules, have led to significant research interest. More recently, attention has been given to conductive MOFs with applications found in electrocatalysis, energy storage and field-effect transistors (FETs), among others.[13,14] MOFs, as a new category of conductive materials, possess properties which situate them perfectly in between conventional organic and inorganic semiconductors. Due to their inherent crystallinity, MOFs may be less affected by disorder than amorphous organic polymers giving improved performance. Furthermore, they possess greater chemical versatility than inorganic semiconductors. In this work, we look at the underlying mechanisms behind X-ray detection in MOFs, considering the material properties required for efficient, highly sensitive, low-noise X-ray detectors. Then, we discuss the current state-of-the-art MOF X-ray detectors, whilst giving perspective on optimised material choices for future MOF X-ray detectors, opening avenues to next-generation detectors and new applications.

2. Mechanisms of X-ray detection

There are two distinct mechanisms employed for ionising radiation detection, termed indirect and direct detection. The two are differentiated by their mechanism for electrical signal generation (Fig. 1).

2.1 Indirect detection

In an indirect detector, the active material, known as a scintillator, down-converts incident X-ray photons into UV-vis photons. The X-ray generated photoemission, known as radioluminescence (RL), is collected by a photodetector, commonly a

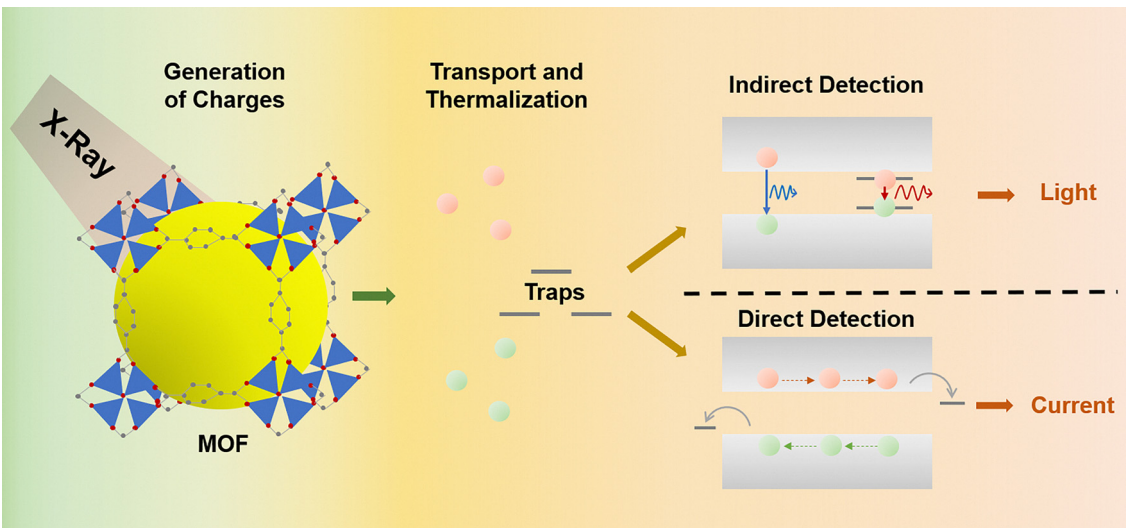

Fig. 1 Free charges are generated by the interaction of the X-ray with the MOF. For indirect detection (scintillation), the incident X-rays are down-converted to photons which are collected by a photodetector. For direct detection, the incident X-rays are directly converted into current which are collected at the electrodes.

photomultiplier tube (PMT) or a-Se photodiode array, to generate an electrical output. Although the exact mechanisms of RL are material-dependent, the mechanism can be generalised into three phases: (i) conversion, (ii) transport, and (iii) radioluminescence.[15] During the conversion phase, incident photons interact with the material lattice, generating electron and hole pairs. The dominating mechanism of interactions between incident photons and the material lattice is highly dependent on the photon energy. Below energies of 100 keV, which are typical of most medical imaging, the photoelectric effect is the dominant mechanism.[16] Compton scattering and pair production are also important mechanisms for electron–hole generation at energies below and above 1 meV respectively.[17] Secondary electrons are then thermalised by electron–electron scattering and Auger processes, leading to the creation of numerous charge carriers. In the transport phase, the large number of electron–hole pairs generated in the conversion phase migrate through the material lattice to the luminescence centre.

The transport phase offers the most substantial chance of light yield losses due to non-radiative recombination of charge carriers *via* trapping at defects, such as ionic vacancies and grain boundaries. Non-radiative recombination must be sufficiently inhibited by optimising crystal growth and morphology. In the final radioluminescence phase, charge carriers are trapped at luminescence centres leading to radiative recombination and emission of photons in the UV-Vis region.[2,15]

2.2 Direct detection

In direct detection, the conversion phase of detection is comparable to that of indirect detection, where X-ray photons interact with a semiconducting material generating high-energy electrons *via* the photoelectric effect, Compton scattering or pair production, which resultantly deposit their excess energy into the surroundings creating numerous electron–hole pairs. When an electric field is applied, the electrons and holes migrate through the lattice, and are then collected at electrodes to produce an electrical current. This process represents the current mode of operation.[8,18]

Direct ionising radiation detectors have three distinct modes of operation: current mode, pulse mode and mean-square-voltage mode (MSV). The operation mode chosen depends on the specific application and requirements. Current mode is used for high pulse rate applications such as medical imaging and dosimetry.[19] It is required where the time between adjacent radiation events becomes too short to measure each individual quantum of radiation that interacts in the detector, or the current pulses from multiple radiation events overlap. Current mode simplifies these measurements by recording an average current of multiple radiation interactions which depends on the product of the interaction rate and charge per interaction.[20] The MSV mode operates similarly to the current mode. In MSV mode, additional computing elements are added to the readout electronics, resulting in the signal being directly proportional to the event rate and the square of the charge produced in each radiation event.[21] The use of MSV mode is limited to specialized applications such as neutron detection due to its unique characteristic of differentiating between mixed radiation types. This is because with the signal being proportional to the square of the charge per event, the signal output will therefore shift the detector response in favour of the type of radiation, giving the largest average charge per radiation event. Pulse mode is used for applications requiring the properties of individual quanta of radiation. The instrumentation used in pulse mode detectors generates an electrical signal for each individual radiation quantum interacting with the detector material. Pulse mode is unique in its ability to preserve information on the amplitude and timing of individual radiation events, making it especially useful for radiation spectroscopy applications. The rate at which radiation events occur is given by the rate at which each electrical signal occurs. Furthermore, the amount of charge generated due to each individual radiation event is reflected by the amplitude of each signal. Pulse mode has several advantages over current and MSV modes, such as significantly greater sensitivity, lower limits of detection (LODs), as well as the ability to harness information from each pulse amplitude.[22]

3. Material properties of X-ray detectors

The X-ray detection capability of a material for both scintillators and direct detectors is significantly determined by its ability to absorb incident X-ray photons. The X-ray attenuation of a given material can be described by its linear and mass attenuation coefficients.

The linear attenuation coefficient (μ) is a material-dependent constant, which describes the fraction of attenuated incident photons from a monoenergetic beam per unit thickness of a material. It is the total probability of a material absorbing or scattering X-ray or gamma rays, taking into consideration the sum of interactions of the photoelectric effect, Compton scattering, and pair production per unit thickness of a material. The linear attenuation coefficient is dependent on the atomic number and density of the absorbing material and can be calculated using eqn (1), where I is the photon intensity over distance x, I_0 is the initial photon intensity, and μ is the linear attenuation coefficient. The linear attenuation coefficient increases with increasing probability of photoelectric absorption P, which is shown in eqn (2). This shows the linear attenuation coefficient increases with atomic number (Z) and density (ρ), whilst decreases with increasing photon energy (E). Therefore, it is preferential to use materials which contain high Z elements and high density, resulting in greater absorption of X-rays.

$$I = I_0 e^{-\mu x} \quad (1)$$

$$P \sim \rho(Z/E)^3 \quad (2)$$

MOFs tend to have lower attenuation coefficients than commercial alternatives such as CsI:Tl and α-Se, which have values of 2.1 cm^{-2} g^{-1} and ~0.537 cm^{-2} g^{-1} respectively at 100 keV, as calculated using the XCOM database.[23] This is due to low Z elements typically in organic linkers. However, by designing MOFs which contain high Z metal centres such as hafnium, lead or

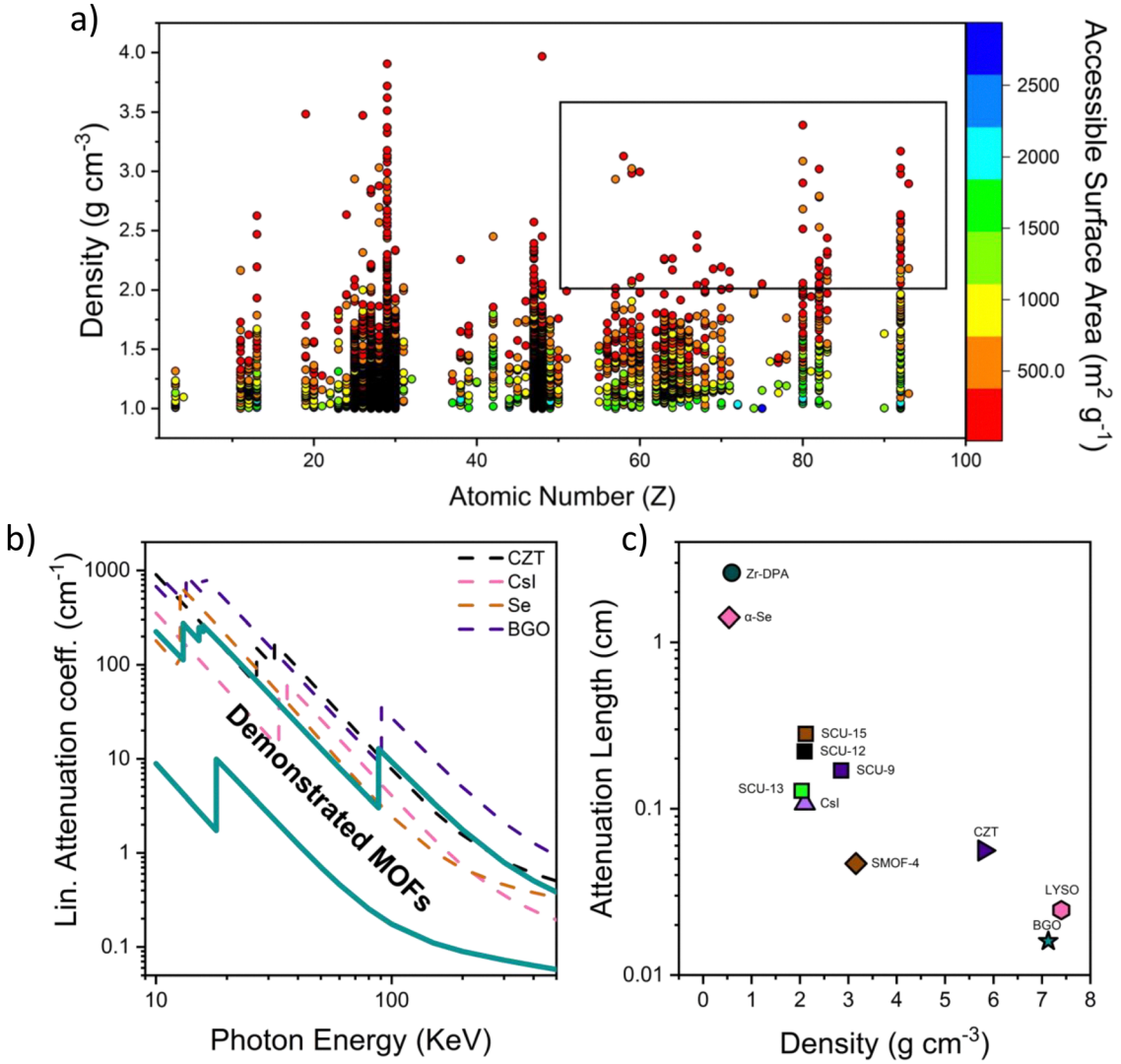

Fig. 2 Comparison of MOF X-ray detection attenuation properties. (a) Synthetic versatility and potential of high-throughput database screening of MOFs for X-ray detection demonstrated using the Cambridge Structural database (non-disordered MOF subset). The plot shows the atomic number, density and accessible surface area of MOFs, with an area highlighted for possible high attenuation MOFs. (b) Linear attenuation coefficients of MOFs used for X-ray detection and commercial materials from 10 to 500 keV. (c) Comparison of density and attenuation length required for 100% attenuation at 100 keV of MOFs used in X-ray detection and commercial materials.

bismuth, respectable stopping powers can be achieved. Currently, in the CSD database over 70 000 MOFs exist with a metal centre with a Z number greater than 50, demonstrating their vast design opportunities.[24] For example, the scintillating MOF, SMOF-4 has a calculated theoretical linear attenuation coefficient of 9.27 cm^{-1} at 100 keV, exceeding that of many commercial detectors (Fig. 2(a)).[25]

The mass attenuation coefficient is another good way to compare materials independently of density and crystal phase. The mass attenuation coefficient is a normalisation of the linear attenuation, where the linear attenuation coefficient is divided by the density of the absorber material (μ/ρ), providing a comparative metric used to assess different materials' potential for ionising radiation absorption. The Beer–Lambert law can be adjusted to accommodate the mass attenuation coefficient, as shown in eqn (3).[26] However, in practice, the density of a material has a significant impact on the linear attenuation coefficients, motivating the use of single crystal and monolithic systems instead of powders.

$$I = I_0 e^{\left(-\frac{\mu}{\rho}\right)\rho x} \quad (3)$$

In this regard, MOF powder densities are typically lower than densities achieved by commercial standards of CsI:Tl and α-Se with densities of 4.51 g cm^{-3} and 4.819 g cm^{-3} respectively. Despite this, over 23 000 MOFs exist with a density greater than 2.0 g cm^{-3} in the CSD. Numerous MOFs have been demonstrated as X-ray detectors, with achievable attenuation lengths for all medical radiation energies, due to their ease of processability (Fig. 2(b)). Furthermore, MOFs are typically synthesised in powder morphologies, with packing densities that are significantly lower than their theoretical crystal density, hindering the competitiveness of MOFs against state-of-the-art

materials such as BGO, which has a density of 7.13 g cm^{-3}. For this reason, a very promising route for increasing the density of MOFs without requiring energy- and time-intensive single crystal synthesis is the development of monolithic systems, which could greatly advance current X-ray detection performance.[27–29] This broad chemical and synthetic versatility gives high potential for the functional design of adaptable, solution-processable and easily scalable detector systems with intrinsically high attenuation efficiencies.

To be commercially viable, detector materials have to maintain consistent performance under continuous operation, with current average lifespans of CT detectors expected to be between 7 to 10 years in the UK. Current CsI:Tl flat panel detectors are warranted up to a dosage of 8730 Gy using <100 keV X-rays, demonstrating the level of stability required. Although the exact energy requirements will change depending on the application, MOFs must have excellent radiation hardness and high stability to hold commercial viability. Although results on the radiation hardness of MOF detectors as X-ray detectors are limited, preliminary results indicate they can be highly tolerant to ionising radiation. For example, Al Lafi *et al.* reported the FTIR analysis of the MOF MIL-101(Cr), with minimal chemical changes seen under 30 kGy of gamma irradiation.[30]

Unprecedented radiation resistance of a thorium-binaphthol MOF (TOF-16) under γ-rays and 5 MeV He^{2+} ions was further demonstrated by Gilson *et al.* Using X-ray diffraction data, TOF-16 showed no bulk structural damage up to a total dose rate of 4 MGy of γ-rays and early onset of crystallinity loss at 15 MGy using He^{2+} ion irradiations.[31] Impressive levels of radiation stability have also been demonstrated in the quintessential MOFs, ZIF-8, UiO-66 and HKUST-1, exhibiting excellent potential for MOFs in radiation detection applications.[32,33] Although MOFs have demonstrated outstanding structural radiation hardness, more data is required on their performance stability under radiation.

Only two scintillating MOFs made from $M_6(\mu_3\text{-}O)_4(\mu_3\text{-}OH)_4(\text{carboxylate})_{12}$ secondary building units (where M is Hf or Zr) and anthracene-based dicarboxylate bridging ligands have been tested for long-term performance under ionising radiation. These two MOFs showed no substantial decrease in X-ray stimulated luminescence after a cumulative dose of up to 300 Gy, the equivalent dose of approximately 1.5 million chest X-rays.[3,34] Although these results suggest that MOFs demonstrate no significant material degradation, more extensive research on their tolerance to X-rays and γ-rays is required to validate the performance of each detector comprehensively.

4. MOF scintillators

MOFs have demonstrated promise as scintillating materials to detect ionising radiation, including neutrons, protons, X-rays and γ-rays. Scintillation, also known as radioluminescence, refers to the emission of radiation upon the absorption of ionising radiation. Existing scintillators frequently use bulk and nanostructured inorganic crystals, polymers, and organic chromophores, with limited control over their quantum efficiency and scintillator response times. In contrast, using fluorescent MOFs as scintillators allows the flexible tuning of properties, for example, *via* the choice of coordinating organic ligands that link the metal clusters.[35]

There are three key material-focussed figures-of-merit for efficient scintillators: (1) efficient light yield, (2) fast response times, and (3) sensitivity to low dose rates.

4.1 Efficient light yield

Light yield can be quantified in two ways. The absolute light yield refers to the ratio of total energy of scintillation photons to the energy deposited by ionising radiation in the scintillator, while technical light yield refers to the total energy of scintillation photons which manages to pass through the window of the detector, to the energy deposited by ionising radiation in the scintillator.

In general, scintillation can originate from ligands (anthracene, naphthalene, stilbene, *etc.*) and from metal centres (such as lanthanides) in MOFs. Various reports in the literature have employed a range of strategies to increase the light yield and obtain efficient scintillation performance.

4.1.1 Scintillations originating from ligands (anthracene, naphthalene, stilbene). Common classes of organic crystal scintillators include anthracene, naphthalene, and stilbene. Other examples include *p*-terphenyl, salicylamide, triphenyl benzene, tetraphenyl butadiene, and 9-phenylcarbazole.[36] For organic crystal scintillators, the scintillation mechanism is due to electron transitions in the π-molecular orbitals. Specifically, the absorption of radiation leads to π-electron ionization. Singlet and triplet states are filled when ions recombine. Non-radiative decay occurs to the first excited state S_1, followed by radiative decay to lower electronic levels.[37] Anthracene crystals have shown the highest light yield among organic scintillators.[22] Ligand-based scintillating MOFs have been developed recently, and the variation of coordinating organic ligands presents a way to tune the scintillating properties. An example of anthracene-based scintillating MOFs is reported in ref. 1. Despite fast luminescent times, the propensity of anthracene to dimerise upon exposure to ionising radiation hinders its scintillation efficiency. Mathis *et al.* propose a strategy of isolating anthracene in dense 3D MOF structures with little or no voids, to overcome this issue and minimise the non-radiative pathways, while ensuring structural stability and rigidity. 9,10-Anthracenedicarboxylate (ADC) was chosen as the linker.[38] Lanthanide metal ions were chosen as they favour high and variable coordination numbers, and can also enhance the X-ray attenuation efficiency due to their heavy metal nature.[39] The authors investigated the following two compositions of 3D networks crystalized in the triclinic system with the $P\bar{1}$ space group: (i) $\{\{[Ln_2(ADC)_3(DMF)_4\cdot DMF]\}_n$, Ln = Eu and Tb} and (ii) $\{\{[Ln_2(ADC)_3(DMF)_2(OH_2)_2\cdot 2DMF\cdot H_2O]\}_n$, Ln = Er and Tm}. Ligand-based proton ion beam-induced luminescence was demonstrated with minimal self-absorption.[22] Prior to their work, 5,5′-(anthracene-9,10-diyl)diisophthalate of

Zn-PCN-14 is the only anthracene-based MOF with reported scintillation behaviour.

Instead of using anthracene ligands, Lu *et al.* demonstrated lead(II)-based scintillating MOFs with naphthalene ligands.[25] Since Pb has a higher atomic number than Hf and Zr, heavy metal lead(II) centres are chosen as effective X-ray absorbers. The ejected photoelectrons undergo inelastic scattering within the framework and secondary chain reactions, followed by energy transfer to the luminescent rigid naphthalene dicarboxylate.

4.1.2 Scintillations originating from metal centers (such as lanthanides). Scintillations can also originate from metal centers. Wang *et al.* report highly efficient X-ray to green light luminescence visible by the naked eye, using uranium as a metal center.[40] Uranium is chosen due to its high atomic number (the heaviest naturally occurring element) and high oxidation number, giving it an X-ray attenuation efficiency better than other common heavy elements like tungsten, thallium, bismuth, and lead (Fig. 3(a)). Apart from an intense Laporte-permitted intrinsic uranyl emission from the lowest excited state to the ground state induced by X-ray irradiation, the compound also demonstrates high radiation hardness (up to 200 kGy of ^{60}Co gamma source) and hygroscopic hardness. A comparison of radioluminescence under various doses, against commercially-available CsI:Tl, is depicted in Fig. 3(b).

Recently, an exceptional photoluminescence quantum efficiency of 92.68% was reported for a lanthanide MOF, (Hphen)-$[(UO_2)_2Eu(BETC)_2]$ (Hphen = protonated 1,10-phenanthroline, BTEC = 1,2,4,5-benzenetetracarboxylic acid), in a heterobimetallic uranyl–europium organic framework. This was achieved using a uranyl sensitization approach, with near unity energy transfer efficiency from UO_2^{2+} to Eu^{3+}. Coupled with a low detection limit of 1.243 $\mu Gy_{air}\ s^{-1}$, this showcases its promise as a scintillator.[42]

In a separate work, a cluster-based antenna sensitization strategy was devised to obtain a series of lanthanide(III)-Cu_4I_4 heterometallic organic framework-based X-ray scintillators. Here, the Cu_4I_4 clusters absorb the X-ray energy, and eventually sensitize Ln^{3+} ions *via* metal-to-ligand charge transfer combined with halide-to-ligand charge transfer, followed by excitation energy transfer. The scintillators demonstrated several desirable properties: high resistance to humidity and radiation, excellent linear response to X-ray dose rate, a high X-ray relative light yield of 29 379 ± 3000 photons MeV^{-1}, and a low detection limit of 45.2 $nGy_{air}\ s^{-1}$. The Tb-Cu_4I_4 scintillator film also exhibited a high spatial resolution of 12.6 lp mm^{-1}.[43]

4.2 Fast response times

Fast scintillators with a response time of tens of picoseconds are necessary for high-resolution medical imaging with a spatial resolution of a few millimetres, for example, in positron emission tomography (TOF-PET). Perego *et al.* demonstrated an ultrafast scintillation rise time of ~50 ps by embedding MOF nanocrystals, comprising zirconium oxo-hydroxy clusters, in a

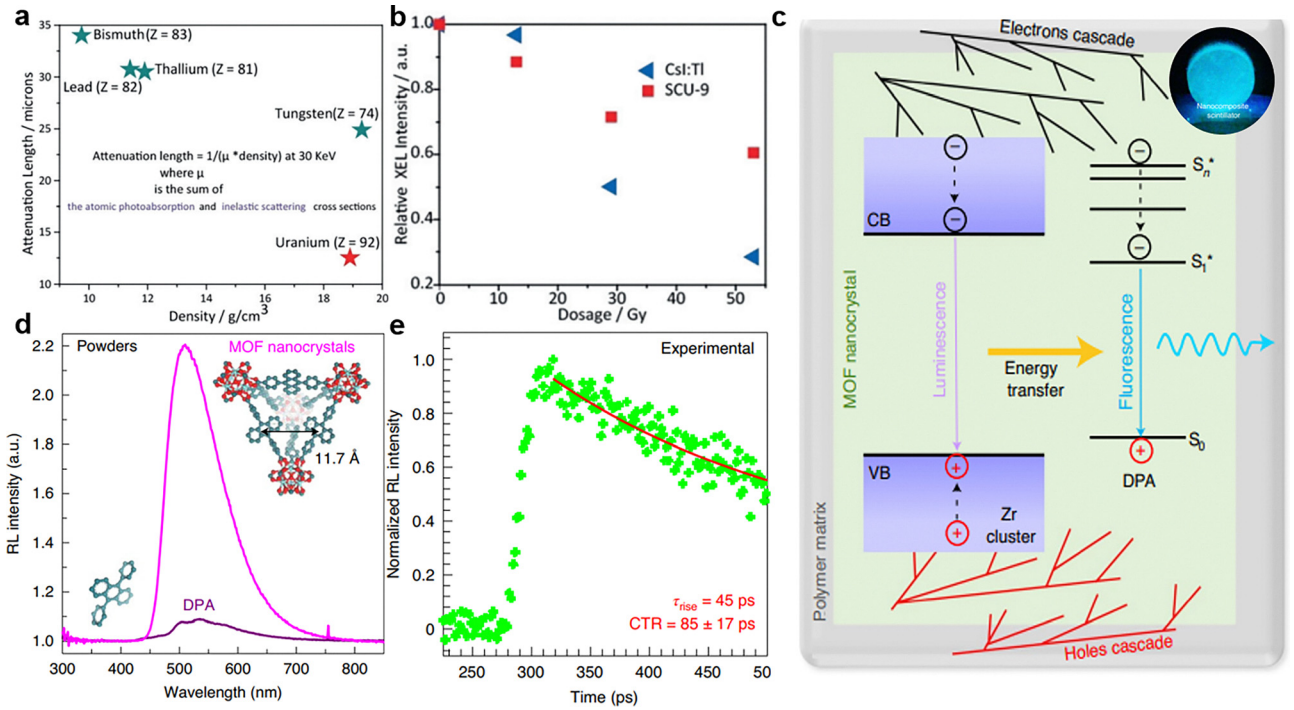

Fig. 3 (a) Comparison of X-ray attenuation efficiency (inversely related to the attenuation length) for several heavy elements. (b) Comparison of X-ray luminescence between the developed uranyl crystal (SCU-9) and a commercially available scintillator (CsI:Tl). Reproduced with permission from ref. 40. (c) Schematic of the scintillation process, which starts with free charges created from the interaction of ionising radiation with the composite scintillator. Inset: An image of the composite scintillator, fabricated by embedding MOF nanocrystals in a polymer matrix, under X-ray irradiation. (d) Steady-state radioluminescence spectra of MOF crystals *versus* DPA. (e) Pulse rise time, at 480 nm, under pulsed X-ray excitation, where the data points (green dots) are fitted with a bi-exponential decay function (red line). Reproduced with permission from ref. 41.

polymer matrix (PMMA and PDMS).[41] Scintillating dicarboxy-9,10-diphenylanthracene (DPA) is used as the ligand due to its high fluorescence quantum yield and the avoidance of re-absorption. Zirconium offers the advantages of chemical and thermal stability. The response time is an improvement compared to ~200–300 ps in commercial devices based on the coincidence time resolution method.

The scintillation mechanism is illustrated in Fig. 3(c). Free charges, created when ionising radiation interacts with heavy elements in the composite, recombine and act to sensitise the creation of singlet molecular excitons on the nearby-anchored ligands, which undergo radiative recombination and fluoresce. The radioluminescence spectrum of the MOF nanocrystals, *versus* pure DPA, under continuous X-ray irradiation is shown in Fig. 3(d). The decay and rise times under pulsed X-ray excitation are 4.1 ns and 45 ps respectively (Fig. 3(e)). This leads to an excellent coincidence time resolution as low as 85 ps, which can compete with other traditional and nano-structured materials. In addition, radiation hardness up to 5.5 kGy exposure dose and high scintillation efficiency are demonstrated. This example illustrates the promise of MOFs for advanced medical-imaging technologies.

4.3 Sensitivity to low dose rates

The detectable dose rate is quantified in nGy_{air}. The development of highly sensitive scintillators, which can improve image resolution while lowering patient dosage, is required for new medical imaging techniques, including single-photon computed tomography (SPCT), computed tomography (CT) and positron emission tomography (PET). Traditionally, scintillators made from lanthanides or heavy atoms face numerous challenges in this regard, necessitating new scintillation candidates. While semiconductors like halide perovskites can achieve comparable imaging performance with commercially available detectors, their detection limits are still widely varied.[44–46] Additionally, perovskite materials typically have poor ambient stability and are prepared under inert conditions, with difficulty scaling up.[47,48]

Gao *et al.* demonstrated Ln(III)-based MOFs with X-ray dosage rate detection limits up to 2.032 $\mu Gy_{air}\ s^{-1}$ for 2D $[Eu_2(1,4\text{-ndc})_3(DMF)_4]_n{\cdot}nH_2O$ and 3.349 $\mu Gy_{air}\ s^{-1}$ for 3D $[Eu_4(2,6\text{-ndc})_6(\mu_2\text{–}H_2O)_2(H_2O)_4]_n{\cdot}2nH_2O$ compounds, superior to the standard for medical X-ray diagnosis dosage rate of 5.50 $\mu Gy_{air}\ s^{-1}$.[49] The absorbed energy from the excited triplet states of the organic ligand molecules can be transferred efficiently to the resonance emission levels of Eu(III) ions. This report demonstrates the prospects of scintillating MOFs for sensitive X-ray detection and high-resolution radiative imaging.

In another example, a highly efficient Förster energy transfer strategy of nearly 100% is employed between a luminescent MOF and a thermally activated delayed-fluorescence organic emitter, giving rise to a high-performance X-ray imaging scintillator.[50] Organic scintillators generally possess good stability and relative ease of processability; however, they are less effective for more energetic X-rays due to their limited effective atomic number, and they exhibit relatively weak luminescence. This poses a bottleneck for their detection sensitivity and imaging resolution. Wang *et al.* successfully overcame this challenge *via* the energy transfer strategy, as well as by employing TADF chromophores as luminescent centers to directly harness both singlet and triplet excitons upon X-ray irradiation.[50] The efficient energy transfer arises from the ultra-short distance and strong spectral overlap between the Zr-fcu-BADC-MOF nanoparticles and the TADF chromophore. The fabricated X-ray imaging scintillator achieved a low detection limit of 256 $nGy\ s^{-1}$, and an imaging resolution of a few hundred micrometers. The detection limit is over 20 times lower than that required for typical medical examinations, showcasing the potential for X-ray radiography. The radioluminescence mechanism is illustrated in Fig. 4(a).

Another advantage of scintillating MOFs is their lower preparation costs as compared to traditional inorganic and organic scintillators, and the potential for desired mechanical properties to be incorporated during the synthesis process, to realise compact and flexible detectors for commercialisation. Inorganic bulk scintillators, including NaI:Tl, CsI:Tl, $PbWO_4$ (PWO) and $Bi_4Ge_3O_{12}$ (BGO), typically require prolonged growth processes under demanding conditions, such as the Czochralski and Bridgman–Stockbarger methods.[53–55] They may have also poor hygroscopic resistance, therefore requiring costly and bulky assembly. In ref. 51 a scintillating 1D MOF was prepared by a low-cost and short-cycle solvothermal process. The 6.0 × 6.0 cm^2 scintillator film achieves a moderately high spatial resolution of 5.5 $lp\ mm^{-1}$ (distinguishable line pairs per millimetre), strong radiation stability with no light quenching despite continuous exposure to an X-ray dose rate of 12.40 $mGy\ s^{-1}$ for 9 h per day for five days, good humidity resistance and thermal stability. The line pairs are considered to be distinguishable when the modulation transfer function exceeds 0.2. The scintillator film is also mechanically flexible, and can be used for non-planar X-ray imaging, or integrated into a flexible matrix or portable and wearable device. Additionally, under X-ray exposure, bright green emission visible to the naked eye is observed, with a rapid decay time of 2.9 ns, and a PLQE of 19.4%. Photographs of the flexible Pb-MOF film are shown in Fig. 4(b). Another example of a 1D X-ray responsive Pb(II)-based scintillating coordination polymer prepared *via* a low-temperature solvothermal method is shown by Xi *et al.*[53] In a separate work, Peng *et al.* constructed a copper iodide cluster-based MOF scintillator. A rod-like microcrystal was prepared by adding polyvinyl pyrrolidone during the *in situ* synthesis process, which improves the radioluminescence efficiency and processability. A scintillator screen made from the microcrystal demonstrates excellent flexibility and chemical stability, and is able to dynamically image the internal structure of flexible materials in extremely humid environments and with a high resolution of 20 $lp\ mm^{-1}$.[56] All these advantages show the potential of scintillating MOFs as promising candidates for practical X-ray imaging, and the additional benefits they bring compared to traditional scintillators.

Several methods can be adopted to further enhance the performance of MOF-based scintillators. MOFs represent a versatile platform with a range of parameters that can be tailored to improve the efficiency and speed in the detection

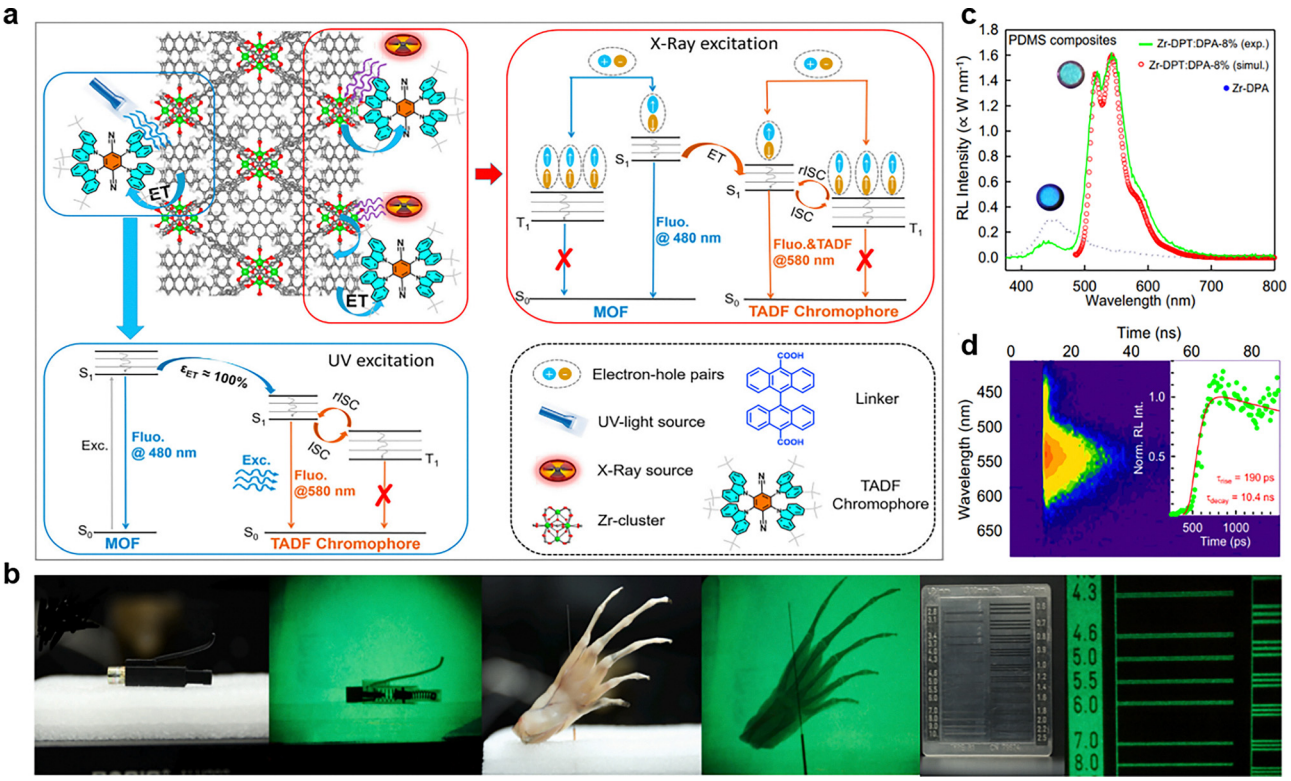

Fig. 4 (a) Illustration of the radioluminescence mechanism, with highly efficient energy transfer from the Zr-fcu-BADC-MOF to the TADF chromophore, under ultraviolet-light irradiation. The acronyms are: ET (energy transfer); ISC (intersystem crossing); rISC (reverse intersystem crossing). Reproduced with permission from ref. 50. (b) The developed Pb-MOF scintillating film, applied in a simple X-ray imaging system, on a commercial lighter (left), bullfrog claw (middle), and line pairs card (right), under 50 kV X-ray irradiation. The spatial resolution achieved was 5.5 lp mm^{-1}. This value is superior to 1.1 lp mm^{-1} obtained using another composite film of an organic anthracene scintillator. Reproduced with permission from ref. 51. (c) Experimental radioluminescence spectrum of nanocomposites with hetero-ligand Zr-DPT:DPA-8% (red) and homo-ligand Zr-DPA nanocrystals (blue), with PDMS as the host polymer matrix. The simulated radioluminescence spectrum is also shown (green). (d) 2D map of composite scintillation emission. Inset: Scintillation pulse with an average decay time of 10.4 ns. Reproduced with permission from ref. 52.

of radiation (comparable to commercial organic and plastic scintillators), while maintaining chemical and thermal stability, as well as radiation hardness. Other desirable properties include a large X-ray attenuation efficiency, and hygroscopic hardness. The chemical composition of the metal clusters and coordinating organic linker molecules, the interchromophore coupling, and the crystalline framework and porous structures, can all be engineered to fit specific applications. For example, Feng *et al.* investigated a series of scintillating MOFs comprised of the linker groups 4,4′-biphenyldicarboxylic acid (H_2BPDC) and 2,6-naphthalenedicarboxylic acid (H_2NDC), and incorporated the electron donor *N*,*N*-diethylaniline (DEA) as an extrinsic dopant within the MOF pores to modify the luminescence characteristics.[57] Two classes of MOF families are explored by the authors: 'isoreticular' MOF with identical cubic framework topologies, and Materials of Institut Lavoisier (MIL).

To enhance the interaction with ionizing radiation, higher density elements, such as hafnium, could be used.[58] High-atomic-number elements interact better with ionizing radiation. The outer-shell electrons of the heavy metal ions are ejected as fast photoelectrons, which first undergo inelastic scattering in the framework, before sensitising the ligand luminescence. Composition engineering can also be considered, with various compounds interacting selectively with different types of radiation. In ref. 34, Hf- and Zr-based MOFs are constructed with anthracene-based dicarboxylate bridging ligands. The attenuation coefficient ranges for Hf from ~110 to 18 $cm^2\ g^{-1}$ and for Zr ~ 23 to 16 $cm^2\ g^{-1}$ in the 15–30 keV range. The synergistic effect of the high *Z* metal clusters and emissive bridging ligands leads to highly efficient radioluminescence. In another study, a Zr-based MOF nanoflower material $Zr_6(\mu_3\text{-}O)_4(\mu_3\text{-}OH)_4(OH)_6(TCA)_2(H_2O)_6$ (H_3TCA = tricarboxylic acids 4,4′,4″-nitrilotribenzoic acid) was synthesised. Intensity-tunable radioluminescence can be achieved by accommodating different guest molecules like xylene and RhB in the same MOF material.[59]

To enhance the scintillation quantum yield, multi-emitter MOF nanocrystals can be used, with minimal self-absorption. For example, Perego *et al.* obtained high efficiency luminescence of 60% with a significant Stokes shift up to 750 meV in crystalline hetero-ligand MOF nanocrystals.[52] The strategy adopted was to co-assemble tetracene-bearing fluorescent moieties with anthracene-based linkers, by zirconium oxy-hydroxy clusters, to tailor the emission properties. The radioluminescence spectrum, with PDMS as the host polymer matrix, under X-ray irradiation is shown in Fig. 4(c). A 2D map of the composite scintillation emission under pulsed X-ray exposure is also depicted in Fig. 4(d), with a decay time of 10.4 ns.

Table 1 summarizes the performance of some reported MOF-based X-ray scintillators. For additional discussion on the figures of merits of X-ray scintillators, we refer the reader to ref. 60.

5. MOF direct radiation detectors

The majority of medical radiation detectors available today still use scintillators as their method of conversion, due to limitations such as high dark currents in current commercial direct detectors hindering their expansion into medical imaging. For example, HgI_2 and PbI_2 detectors have large leakage currents; Si and a-Se devices due to their low atomic number (Z) have low X-ray stopping power; and CZT-based systems usually have non uniform charge transport and large noise levels due to charge trapping.[7,8] However, compared to scintillators, direct radiation detectors, which use a semiconductive material to directly convert ionizing radiation into charge carriers which are ultimately collected under bias, pose several advantages, such as improved responsivity, and higher spatial and energy resolution.[62] Furthermore, some direct detector systems including CZT have shown promise for photon counting direct detection, processing X-ray signals from each individually-deposited photon separately, leading to spectral X-ray detectors.[63] Various other materials have been reported as promising direct radiation detectors over recent decades, including amorphous Se, crystalline Si, as well as halide perovskites which have recently gathered significant research attention.[60,62,64,65] These materials still face significant limitations, for example a-Se and Si both possess low radiation attenuation efficiencies, particularly at high energies, limiting their use to applications requiring X-ray energies below 40 keV.[22,66] Furthermore, halide perovskites are still hindered by large current drifts requiring long stabilisation (turn on) times, and inherent instabilities in ambient air. Although the research area of semiconductive MOFs still lags in terms of applications in energy storage, drug delivery and catalysis, recent studies have shown highly promising opportunities to design multifunctional MOF radiation detectors (Table 2). This is due to their design versatility, high stabilities, and potential to be integrated into flexible devices, opening opportunities for improved non-planar imaging, reducing radiation exposure times, and non-destructive inspection imaging. There are several key figures of merit for direct radiation detectors, including sensitivity (S), charge collection efficiency (CCE), dark current, limit of detection (LOD), and response speeds.

5.1 Sensitivity

The sensitivity of an X-ray detector is one of the primary figures of merit determining the detector's effectiveness. The sensitivity of direct detectors can be described as the charge collected per unit exposure of incident radiation per unit area. The sensitivity can be calculated using eqn (4), which relates the photocurrent (I_p), dark current (I_D), radiation dose rate in air of the X-ray (D) (measured in $Gy_{air}\ S^{-1}$) or radiation exposure (measured in R s^{-1}) and the effective area of the detector (A).

$$S = \frac{I_p - I_D}{D \times A} \quad (4)$$

Care should be taken when comparing quoted sensitivities due to the dependence of sensitivity on the incident radiation energy and applied electric field. The record sensitivity for a MOF-based direct radiation detector was reported by Yu *et al.* in 2024.[67] Here, a viologen-templated Dy(III)-based MOF with radiochromic semiconductive properties is reported with excellent sensitivity. The synthesised MOF RCS-2, $a_2(EV)_{0.5}[Dy_2(IPA\text{-}SO_3)_4]\cdot H_2O$ (RCS-2; IPA-SO_3 = 5-sulfoisophthalate; EV^{2+} = *N*,*N*′-diethyl-4,4′-bipyridinium cation) shows an X-ray sensitivity of 6385 μC Gy^{-1} cm^{-2} under a bias of 271 V cm^{-2} and source current of 50 kVp. This work builds upon the group's previous works from Han *et al.* in 2022, where they present the first rewritable radiochromic semiconductive MOF, $\{(EV)[Zn_2(ox)_3]\cdot 3.5H_2O\}_n$ which exhibited an impressive X-ray sensitivity of 3216 μC Gy^{-1} cm^{-2} under a X-ray tube voltage of 30 kVp and bias of approximately 238 V mm^{-1}.[68]

The importance of MOF chemical structure design is highlighted, with the transportation of charges significantly influenced by intermolecular interactions. In the case of RCS-2, the numerous delocalised conjugated π-electrons, highlight the advantage of a high number of robust π–π interactions, mitigating energy losses and aiding rapid charge transport.

The use of conjugated frameworks for MOF direct detectors was also shown by Li *et al.* who demonstrated promising X-ray detection performance with the lead-free MOF, Ni-DABDT. This MOF comprised of Ni and DABDT (2,5-diamino-1,4-benzenedithiol dihydrochloride) forming a p–d conjugated MOF which exhibited a good sensitivity of 98.6 μC Gy^{-1} cm^{-2} under 50 kVp X-ray energy and a low operating bias of 1 V. The low operating bias of 1 V has significant promise for developing handheld devices, with higher sensitivities expected at increased biases.[69] This also shows the potential of non-toxic, low Z atom MOFs as low-cost, solution-processable alternatives to current commercial detectors.

Furthermore, the incorporation of photochromism active guest species is an excellent example of host–guest interactions in MOFs, used to aid application specific properties. In the case of photochromism active cations, these species are known to improve charge separation and promote conductivity, significantly enhancing MOF charge collection efficiency and sensitivity. This opens up numerous avenues of exploration to improve performances of MOFs increasing competitiveness with leading materials such as single crystal CdTe/CZT and halide perovskites.

These examples demonstrate methods which can be used to increase the sensitivity of MOFs. Sensitivity in MOF direct detectors has been a particular challenge. Although sensitivities have now increased beyond commercial a-Se detectors (20 μC Gy^{-1} cm^{-2}) and polycrystalline CZT (2400 μC Gy^{-1} cm^{-2}) at 20 kVp and 104 V mm^{-1} fields and 80 kV and 250 V mm^{-1} respectively, they still lag behind the top performing perovskite direct X-ray detectors.[64,65]

Table 1 Performance comparison of some MOF-based X-ray scintillators

Material	Crystal system (space group)	Density ($g\ cm^{-3}$)	PL wavelength (nm)	PL decay time (ns)	RL wavelength (nm)	Limit of detection ($\mu Gy_{air}\ s^{-1}$)	Radiation and operational stability	Other info	Ref.
$[Pb(1,4\text{-ndc})\ (DMF)]_n$	Orthorhombic ($P2_12_12_1$)	2.193	494	1.61	512, 550, 600	—	—	—	25
$[Pb(1,4\text{-ndc})(DMA)]_n$	Orthorhombic ($P2_12_12_1$)	2.187	451	13.45	512, 550, 600	—	—	—	
$[Pb_2(2,6\text{-ndc})_2(H_2O)]_n{\cdot}n$DMF	Triclinic ($P\bar{1}$)	2.380	390	3.98	398, 508, 509, 545	—	—	—	
$[Pb_4(2,6\text{-ndc})_3Cl_2]_n$	Monoclinic ($P2_1/c$)	3.154	434, 536, 578, 633	32.95–47.15 μs	539, 576	—	—	—	
$Hf_6(\mu_3\text{-O})_4(\mu_3\text{-OH})_4(carboxylate)_{12}$	—	—	470	6.19	480	—	Up to 300 Gy cumulative dose	—	34
$Zr_6(\mu_3\text{-O})_4(\mu_3\text{-OH})_4(carboxylate)_{12}$	—	—	470	5.96	480	—		—	
$\{[Eu_2(ADC)_3(DMF)_4{\cdot}DMF]\}_n$	Triclinic ($P\bar{1}$)	1.645	440	(Overlap with IRF)	440, 460	—	—	—	38
$\{[Tb_2(ADC)_3(DMF)_4{\cdot}DMF]\}_n$	Triclinic ($P\bar{1}$)	1.681	435	0.3	445	—	—	—	
$\{[Er_2(ADC)_3(DMF)_2(OH_2)_2{\cdot}2DMF{\cdot}H_2O]\}_n$	Triclinic ($P\bar{1}$)	1.697	430	(Overlap with IRF)	475	—	—	—	
$\{[Tm_2(ADC)_3(DMF)_2(OH_2)_2{\cdot}2DMF{\cdot}H_2O]\}_n$	Triclinic ($P\bar{1}$)	1.703	430	(Overlap with IRF)	—	—	—	—	
$UO_2(HL)(H_2O)$	Monoclinic ($I2/a$)	2.88	490, 512, 536, 562	—	490, 512, 536, 562	—	Up to 200 kGy dose	—	40
Zr-DPA:PMMA	Cubic ($Fm\bar{3}m$)	—	450–485	4.0–5.3	485	—	Up to 5.5 kGy dose	SRT: 295 ps, SDT: 2.9 ns	41
Zr-DPA:PDMS	Cubic ($Fm\bar{3}m$)	—	464–485	3.7–4.4	485	—		CTR: 85 ps, SRT: 275 ps, SDT: 2.8 ns	
$[Eu_2(1,4\text{-ndc})_3(DMF)_4]_n{\cdot}nH_2O$	Triclinic ($P\bar{1}$)	—	614, 618	—	592, 617, 695	2.032	Up to 30 Gy dose	—	49
$[Eu_4(2,6\text{-ndc})_6(\mu_2\text{-}H_2O)_2(H_2O)_4]_n{\cdot}2nH_2O$	Monoclinic ($P2_1/n$)	—	611, 616	—	591, 615, 701	3.349		—	
Zr-fcu-BADC-MOF	—	—	600	—	575	0.256	Up to 0.70 Gy dose	—	50
$[Pb(adda)(DMF)]_n$	Monoclinic ($P2_1/c$)	—	512	2.9	512	—	Up to 230 °C, 151 Gy dose	—	51
Hetero-ligand Zr-DPT:DPA-8% composite in PDMS matrix	Cubic ($Fm\bar{3}m$)	—	540	10.9	430, 540	—	Up to 50 °C, ∼100 Gy dose	Scintillation yield: 5000 ph MeV^{-1}, SRT: 190 ps, SDT: 10.4 ns	52
IRMOF-10	—	—	400	5.4, 15.0	400	—	—	Zn_4O metal cluster nodes and $BPDC^{2-}$ linker groups	57
IRMOF-8	—	—	400	4.7, 16.9	476	—	—	Zn_4O metal cluster nodes and NDC^{2-} linker groups	
Linear chains of Al(OH) metal clusters connected into a 3D framework by NDC^{2-} linkers	—	—	381	—	—	—	—	Open complex	
	—	—	471	—	479	—	—	Closed complex	
IRMOF-8 with *N*,*N*-diethylaniline trapped within the pores	—	—	559	—	400, 475, 545	—	—	Zn_4O metal cluster nodes and NDC^{2-} linker groups	
Hf-dicarboxy-9,10-diphenylanthracene	—	0.6–0.7	490	2.4	500	—	Outperform commercial scintillator EJ-276 with a linear response to ^{85}Kr below 1 $kBq\ m^{-3}$	SRT: Sub-ns, SDT:3 ns	61
Tb-Cu_4I_4	Tetragonal ($I\bar{4}2d$)	2.211	547	1525 μs	547	0.045	—	Relative light yield: 29 379 ph MeV^{-1}	43

Table 1 (*continued*)

Material	Crystal system (space group)	Density (g cm^{-3})	PL wavelength (nm)	PL decay time (ns)	RL wavelength (nm)	Limit of detection (μGy_{air} s^{-1})	Radiation and operational stability	Other info	Ref.
(Hphen)[$(UO_2)_2$Eu(BTEC)$_2$]	Monoclinic ($P2_1/c$)	2.743	613	—	613	1.243	Retains 92% intensity after 53 Gy dose Retains 80% intensity after 95% relative humidity for 2 hours	PLQY 92.68%	42

H_2ADC: 9,10-anthracenediarboxylicacid; DMF: *N*,*N*-dimethylformamide; DPA: 9,10-diphenylanthracene; PDMS: polydimethylsiloxane; PMMA: polymethyl methacrylate; H_2BPDC: 4,4′-*trans*-diphenyldicarboxylic acid; H_2NDC: 2,6-naphthalenedicarboxylicacid; IRMOF: isoreticular MOF; MIL: Materials of Institut Lavoisier; 1,4-H_2ndc = 1,4-naphthalene dicarboxylate; 2,6-H_2ndc = 2,6-naphthalene dicarboxylate; DMA = *N*,*N*-dimethylacetamide; H_3L: trimesic acid; DPT: 5,12-diphenyl-tetracenedicarboxylate; H_2adda = (2*E*,2′*E*)-3,3′-(anthracene-9,10-diyl) diacrylic acid; Hphen: protonated 1,10-phenanthroline; BTEC: 1,2,4,5-benzenetetracarboxylic acid; SRT: Scintillation rise time; SDT: scintillation decay time; IRF: instrument response function; CTR: coincidence time resolution

The potential to overcome these challenges through the bottom-up design of MOF structure and incorporation of guest species is further demonstrated by Wei *et al.*, whose work builds on the emergence of semiconductive multiple hybrid heterojunctions which provide opportunities to design electronic properties through a bottom-up approach. In their work, Wei *et al.* demonstrate the performance and X-ray absorption capabilities of donor–acceptor MOFs can be enhanced using polyoxometalates (POMs), which are excellent building blocks for fabricating high-performance ternary MOF direct X-ray detectors, due to their tunable bandgaps, structure and high Z.[70] In their work, a photoactive POM $[(\alpha\text{-}SiW_{12}O_{40})]^{4-}$ was introduced as a second donor guest species into the binary MOF $\{[Ni{\cdot}bcbp{\cdot}(H_2O)_2]{\cdot}(H_2O)_4{\cdot}Cl\}_n$ (Ni-bcbp, bcbp): H_2bcbp·2Cl = 1,1′-bis(4-carboxyphenyl)(4,4′-bipyridinium) dichloride. This MOF host was developed from the electron-deficient organic ligand viologen which acts as an acceptor and redox-active donor metal Ni. This results in a semiconductive ternary donor–donor–acceptor (D–D′–A) MOF named SiW@Ni-bcbp, which demonstrated enhanced sensitivity of up to 5741.6 μC Gy_{air}^{-1} cm^{-2}. The synergistic effects of the electron reservoir and POM which improve charge separation, photoelectric conversion performance and reduce carrier recombination probability provides promising avenues for future design of MOF direct detectors which can overcome the challenges of sensitivity and push beyond current limits.

The sensitivity of a given detector can also be theoretically calculated by relating the quantum efficiency (η_x), charge collection efficiency (η_{cc}) and number of electron–hole pairs (EHP) created by each absorbed photon (η_m), giving significant insight into potential detector materials, prior to synthesis.[71] The quantum efficiency can be calculated by $\eta_x = 1 - e^{-\mu t}$, where μ is the attenuation coefficient, and t is the thickness of the active layer. η_m is determined by $\eta_m = E\frac{(\mu_{en}/\mu)}{W_\pm}$, where μ_{en} is the energy absorption coefficient and $W_\pm$ is the electron hole pairs (EHPs) creation energy. η_{cc} depends on the product of $\mu\tau F$; where μt is the charge mobility lifetime product and F is the applied electric field, and the geometric design of the detector.[72] Bringing these together, the theoretical sensitivity can be expressed by eqn (5), where S_0 (given in $C\,R^{-1}$ cm^{-2}) is a constant that depends on the X-ray energy (eqn (6)).[73] To convert S_0 into SI units it can be multiplied with f_{conv} = (8.76×10^{-3} Gy_{air} R^{-1}).

$$S = S_0 \eta_x \eta_m \eta_{cc} \quad (5)$$

$$S_0 = \frac{5.45 \times 10^{13} e}{E(\mu_m/\rho)_{air}} \quad (6)$$

It is equally important to the sensitivity of the detector, for the generation of collectable EHPs to be maximised. The amount of collectable charge (ΔQ) generated by the absorbed radiation energy (E) is defined by eqn (7), where e is the elementary charge. From eqn (7), we see that the EHP creation energy ($W_\pm$), defined as the amount of energy required to generate a single EHP, should be as low as possible.[74] From Klein's rule, we know that for many semiconductors $W_\pm \approx 3E_g$ where E_g is the

Table 2 Performance comparison of MOF-based and commercial direct X-ray detectors

Material	Sensitivity ($\mu C\ Gy^{-1}\ cm^{-2}$)	Tube current (kV)	Applied bias (V)	Resistivity ($W\ cm^{-1}$)	$\mu\tau$ product ($cm^2\ V^{-1}$)	Limit of detection ($nGy\ s^{-1}$)	Ref.
SCU-13	65.86	80	100	6.98×10^{10}	4.3×10^{-4}	6553	45
RhB + @TbTATAB	51.90	30–160	100	8.0×10^{11}	1.1×10^{-3}	4420	77
Cu-DABDT	78.7	40	1	—	6.5×10^{-4}	—	78
SCU-12	23.8	80	30	1.6×10^{11}	1.3×10^{-4}	705	79
Ni-DABDT	98.6	50	1	—	3.3×10^{-4}	7200	69
SCU-15 single crystal	3.15	—	1	6.18×10^{11}	2.2×10^{-3}	33 960	80
$\{(EV)[Zn_2(ox)_3]\cdot 3.5H_2O\}_n$	3216	—	30	3.84×10^{9}	8.3×10^{-3}	—	68
RCS-2	6385	50	271	4.31×10^{8}	1.61×10^{-4}	—	67
ZIF-8 Wafer	70.82	20	—	2.88×10^{12}	—	3475	81
α-Se	20	20	—	—	5.0×10^{-10}	5500	64
CdZnTe polycrystalline	2400	80	—	$\sim 10^{9}$	7.0×10^{-9}	50 000	65 and 82
CdTe single crystal	4.2×10^{5}	61	—	—	5.2×10^{-3}		83
HgI_2	2400	80	—	—	5.0×10^{-9}	10 000	84

bandgap.[75,76] Therefore, the use of a material with a narrow bandgap is preferable for maximising charge carrier generation.

$$\Delta Q = \frac{eE}{W_{\pm}} \tag{7}$$

5.2 Charge collection efficiency

Alongside the generation of charge carriers, they must be efficiently transported through the material and collected. The charge collection efficiency is determined by two principal factors: the charge carrier mobility (μ) and the average lifetime of the charge carrier (τ). The sum of these factors ($\mu\tau$) is known as the charge mobility lifetime product. $\mu\tau F$ represents the schubweg distance, the mean distance travelled by the charge carrier before it is trapped or undergoes recombination, where F is the applied electric field. To maximise the charge collection efficiency, it is required that the schubweg distance of the EHPs be greater than the thickness of the active material.[74] It is important to balance the need for improving X-ray attenuation with greater material thicknesses and ensuring schubweg distances remain greater. If the thickness of the material exceeds schubweg distances, charge collection and therefore detector sensitivity will be limited.

Typically, single crystal direct detectors' $\mu\tau$ product ranges from 10^{-4} to $10^{-3}\ cm^2\ V^{-1}$. For example, CZT single crystals have a $\mu\tau$ value of $3.0 \times 10^{-3}\ cm^2\ V^{-1}$, whereas polycrystalline CZT and a-Se have $\mu\tau$ values of $7.0 \times 10^{-9}\ cm^2\ V^{-1}$ and $5.0 \times 10^{-10}\ cm^2\ V^{-1}$ respectively.[64,65,85] The largest $\mu\tau$ products demonstrated in a standalone MOF X-ray detector are shown in the single crystal of MOF SCU-15, (UO_2 ($SC_6H_4COO)_2$(DMF)), which has a calculated $\mu\tau$ product of $2.18 \times 10^{-3}\ cm^2\ V^{-1}$, exceeding that of CZT single crystals, as well as being comparable to some halide perovskite single crystals. The reported SCU-15 demonstrates a millimetre thickness single crystal detector, necessitating the need for a large $\mu\tau$ product, and giving promise of high energy radiation detection, where large thicknesses are required to maximise attenuation. Despite the comparatively large $\mu\tau$ product, SCU-15 has a relatively low X-ray sensitivity of $3.51\ \mu C\ Gy^{-1}\ cm^{-2}$ at 1 V, hindered by the charge collection efficiency in a millimetre-scale device.[80] Further improvements in the $\mu\tau$ products of MOFs were shown by Liang *et al.* which improved the $\mu\tau$ product of TbTATAB ($Tb_2L_2\cdot 4H_2O\cdot 6DMF$, L = $TATAB^{3-}$, 4,4′,4″-*s*-triazine-1,3,5-triyltri-*p*-aminobenzoate, DMF = *N*,*N*-dimethylformamide) from $3.21 \times 10^{-4}\ cm^2\ V^{-1}$ to a record in MOF-based X-ray detectors of $1.12 \times 10^{-3}\ cm^2\ V^{-1}$ by incorporating the electron deficient molecule Rhodamine B (RhB) within the pores of the MOF (Fig. 5).[77] The incorporated guest species demonstrated that the optoelectronic efficiency of MOFs can be improved by controlling the exciton behaviour, resulting in efficient energy transfer from the framework to guest species *via* a Wannier–Mott exciton to Frenkel exciton conversion. Alongside drastically improving the $\mu\tau$ product, RhB^+@TbTATAB exhibits a 44 times increase in sensitivity when compared to TbTATAB at an applied bias of 30 V. The versatility to incorporate guest species with a porous MOF therefore provides substantial opportunity to tune the optoelectronic and thus X-ray detection properties of MOFs, with $m\tau$ products already achieving values in excess of CZT and a-Se, as well as some perovskites such as $MAPbI_3$ wafers ($2 \times 10^{-4}\ cm^2\ V^{-1}$) and $Cs_2AgBiBr_6$ single crystals ($3.75 \times 10^{-3}\ cm^2\ V^{-1}$).[64,86,87] There is huge potential to exceed the best alternatives, opening pathways to cheaper, easily processable and size adaptable radiation detectors.

The effective mass (m^*) of electrons and holes also plays an important role in determining the charge transport properties of semiconductors. The charge mobility is related to m^* by eqn (8), showing it is preferential for smaller m^*:

$$\mu = e\frac{\tau}{m^*} \tag{8}$$

Materials which have similar m^* of electrons and holes are excellent in providing balanced ambipolar conductivity which is also important to device operation. This ensures little disparity between the two types of carriers preventing significant trapping of one carrier. Trapping of either electrons or holes in deep traps will have various detrimental effects on the detector performance. Firstly, there is a reduction in sensitivity due to a lower charge collection efficiency.

Secondly, in a pixelated detector, the trapped charge carriers can induce charges on neighbouring pixels resulting in a reduction of resolution for trapped holes and increase of resolution at high spatial frequencies for trapped electrons.

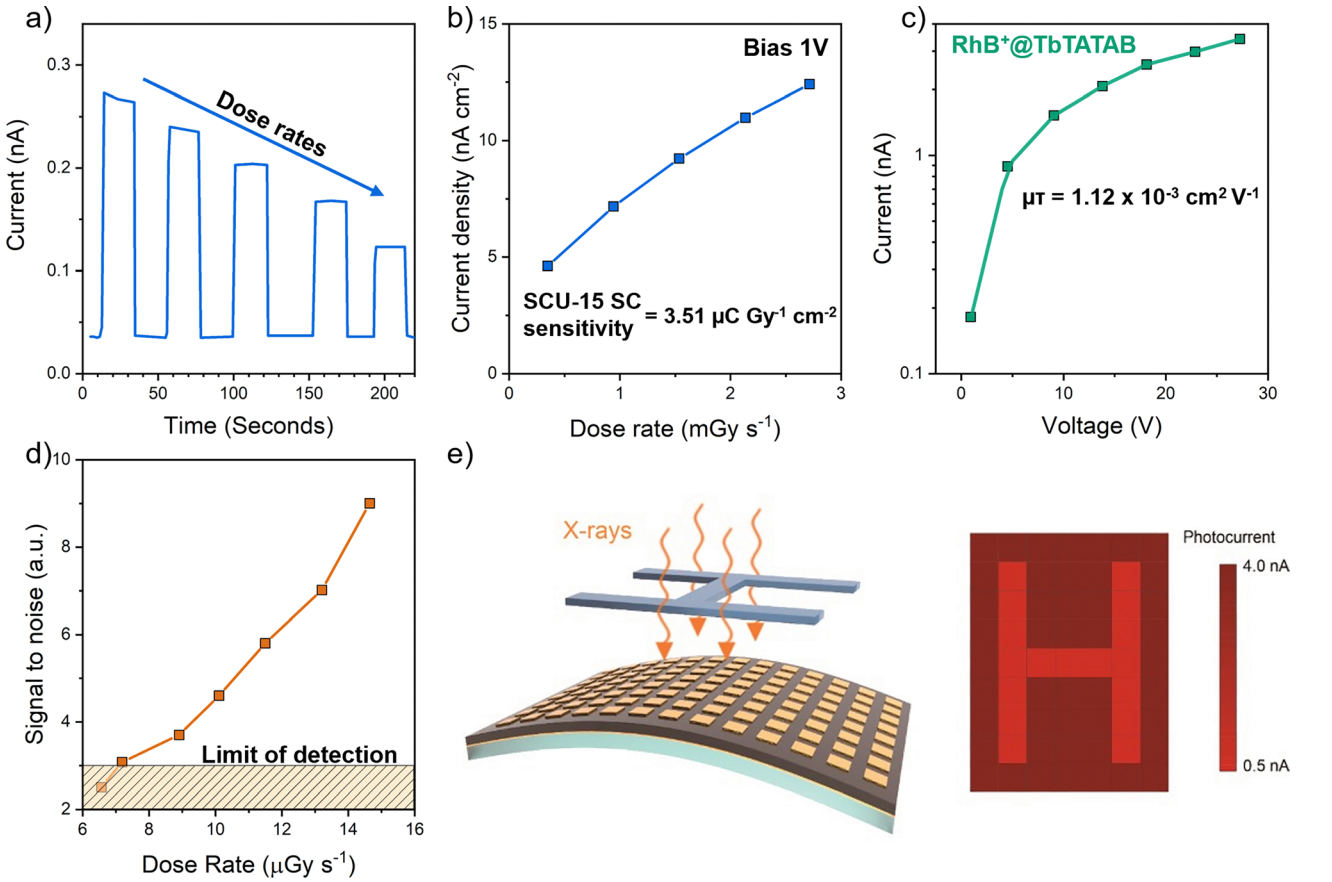

Fig. 5 Summary of direct X-ray characterisation of MOFs. (a) The photocurrent of SCU-15 SC decreased *versus* time under different dose rates from 2.75 to 0.53 mGy s^{-1}. Reproduced with permission from ref. 80. (b) X-ray induced current response with increasing dose rate of SCU-15 SC, and maximum sensitivity measurement. Reproduced with permission from ref. 80. (c) Mobility-lifetime product of best performing mobilities demonstrated in a MOF direct X-ray detector (RhB + @TbTATAB) derived from the photoconductivity curves. Reproduced with permission from ref. 77. (d) X-ray dose-dependent signal-to-noise ratio of the Ni-DABDT detector, with the limit of detection highlighted. Reproduced with permission from ref. 69. (e) Schematic structure of the X-ray prototype imaging device based on the Ni-DABDT material and X-ray imaging of an aluminium bulk with the letter "H" pattern. Reproduced with permission from ref. 69.

Furthermore, recombination of charge carriers with previously trapped holes or electrons will further cause a reduction in sensitivity as well as image ghosting.

Carrier mobilities are also greatly affected by material morphology, crystallinity, and defects. This has been demonstrated in perovskite research where single crystals have demonstrated much greater mobilities over thin films due to reduced trap density and eliminated grain boundaries. Various processing methods to optimise film quality, alongside passivation techniques, have been developed for perovskites and lessons can be taken from this to reduce grain boundaries and defects, optimising mobilities and longer carrier diffusion lengths.

5.3 Dark current

Another important concept for X-ray detectors is dark current, which should be kept as low as possible to maximise the signal-to-noise ratio (SNR). The dark current of a detector is influenced by the number of activated charge carriers generated by the irradiation and the amount of charge carriers injected from the electrodes. The number of injected charge carriers is mainly affected by the electric field strength (F) and the resistivity of the material. The number of intrinsically generated charge carriers is related to $W_{\pm}$ and therefore the bandgap of the material. Reducing the dark current requires the $W_{\pm}$ to be lower, and therefore broader bandgaps are preferred. Nonetheless, this negatively affects device sensitivity and a compromise between achieving both adequate sensitivity and low dark current is required. A wide range of resistivity is seen within MOFs due to their chemical tunability, allowing fine tuning towards a wide range of radiation detection applications. Xu *et al.* developed an ultra-low-dose radiation detector by fabricating ~400 μm-thick ZIF-8 wafers through pelletisation.[81] The detector exhibited exceptionally high resistivity, measured at 2.88×10^{-12} Ω cm^{-2}, approximately two orders of magnitude higher than most other MOFs and commercial direct detectors such as CZT. This high resistivity contributed to an ultra-low dark current of just 1.27 pA mm^{-2} under an electric field of 322 V mm^{-1}. While the ZIF-8 detector demonstrated a modest X-ray sensitivity of 70.82 μC Gy^{-1} cm^{-2}, it achieved a promising image resolution of 1.2 lp mm^{-1}, highlighting its potential for full-scale imaging applications.

Notably, this ZIF-8 detector was the first MOF-based device to be applied for alpha particle detection, achieving an energy

resolution of 43.78% at a 300 V bias. These results, likely enabled by the exceptionally low noise of the ZIF-8 detector, demonstrate its proof-of-concept viability for single-photon counting applications. Such applications include alpha particle detection, gamma spectroscopy, and fast neutron solid-state detection. MOFs could be particularly well-suited for fast neutron detection due to the abundance of hydrogen-rich organic molecules in MOFs, which results in a high frequency of proton recoil events, critical for neutron detection.

The electrical conductivity of the MOF Cu-DABDT (DABDT = 2,5-diamino-1,4-benzenedithiol) was shown by Li *et al.* to have a dramatic temperature dependence with values of 3.7×10^{-7} S cm^{-1} at 300 K to 7.1×10^{-11} S cm^{-1} at 50 K.[78] This temperature-dependent electrical conductivity is seen in similar X-ray detector materials such as the perovskite $Cs_2AgBiBr_6$ and gives the possibility of a new route to optimisation between achieving the required resistivity to ensure low dark currents and maintaining a good sensitivity.[86] Using the temperature-dependent conductivity measurement, the effective activation energy of ion migration can also be calculated (E_a). For Cu-DABDT, the E_a at 300 K was measured to be 242.13 meV which is higher than that of $MAPbBr_3$ and $MAPbI_3$ (<200 meV) indicating a reduction in ion migration in Cu-DABDT, reducing the noise and providing a potentially more stable dark current under higher biases. Furthermore, the Cu-DABDT exhibited excellent sensitivity for a low Z detector of 78.7 μC Gy^{-1} cm^{-2} at a low bias of 1 V and 40 kVp. Techniques such as incorporating MOFs into polymer membranes can also be successfully used to alter the optoelectronic properties of the MOF, optimising their X-ray detection capabilities. For example, Liang *et al.* produced a flexible X-ray detector by incorporating the MOF SCU-13 ($[[(CH_3)_2NH_2]_2PbL_2]$) (L = $C_6Cl_2O_4^{2-}$) into a polyvinylidene fluoride membrane.[45] This resulted in a reduced resistivity of 6.98×10^{10} W cm^{-1} compared to 2.18×10^{11} W cm^{-1} for the pelletised MOF. This results from the homogeneous distribution within the thermoplastic membrane resulting in a reduction in grain boundary resistance compared to the pelletised MOF. This reduction in resistivity, alongside a reduction in trap density from 6.09×10^{10} cm^{-3} in the pelletised MOF to 1.74×10^{10} cm^{-3} in the SCU-13 based thermoplastic membrane results in a 2.34 times greater sensitivity for the SCU-13 membrane compared to the pelletised SCU-13 measured using 80 kVp and 50 V bias.

5.4 Limit of detection

The sensitivity and dark current of a direct radiation detector are intrinsically linked to the detector's limit of detection (LOD), a key metric for evaluating performance under specific conditions such as security imaging or medical dose testing. The LOD is defined as the measurable dose rate that produces a current response of 3 times the dark current or noise level. This therefore gives the minimum radiation dose rate that can be measured accurately by a radiation detector. To achieve a low LOD it is therefore vital to have a sufficiently low and stable dark current, whilst maintaining a high sensitivity and current response. Most MOF direct X-ray detectors have so far typically demonstrated LODs similar to that of α-se (5.5 μGy s^{-1}) and exceeding the requirements for typical medical imaging. The lowest limit of detection recorded for a MOF based direct detector so far was reported by Wang *et al.* in 2019. Wang *et al.* used the MOF SCU-12, $[(CH_3)_2NH_2]Tb_2L_3(DMF)_2(H_2O)_2(HCOO)$, (L = $C_6Cl_2O_4^{2-}$), to form a pelletised polycrystalline direct detector with an excellent LOD of 0.705 μGy s^{-1}, giving great promise for the potential use as MOFs for low dosage radiation detectors.[79] This is a vital need for meeting the increasing demands of modern medicine, where regular preventative medical scans are required.

5.5 Response time

The final key figure of merit for direct radiation detectors is their response speeds. A direct radiation detector's response speed is defined as the rise time of the photocurrent pulse from 10% to 90% (τ_1) and the decay time of the same photocurrent pulse from 90% to 10% (τ_2). Typically, the response speed is closely associated with the trap density of the detector material as well as the device architecture. The response speed of a detector dictates the application it is suitable for to maintain current operational performance. For example, medical radiography and CT scans typically have a decay time of 1000 ns and 2000 ns respectively and longer afterglows of a few milliseconds.[88,89] On the other hand, positron-emission tomography (PET) typically requires a fast response speed of approximately 40 ns.[90] Direct radiation detectors suffer a disadvantage compared to scintillators with respect to response speeds, with typically slower response speeds, requiring careful optimisation of materials to reduce trap densities and appropriate choice of application for the detector material.

6. Opportunities to overcome challenges and new applications for MOF-based X-ray detectors

6.1 Leveraging chemical versatility to enhance performance

MOFs are increasingly being recognized as potential candidates for next-generation X-ray detectors. Their chemical versatility and tunability allow for sophisticated and rational design of MOFs for radiation detection, by varying ligands, metal centres, and guest species incorporated within their permanent porosity. This has led to the development of over 100 000 experimentally synthesized MOFs in the Cambridge structural database, with almost infinite theoretical possibilities for new MOFs.

The permanent porosity of MOFs, although limiting for density and radiation attenuation, is beneficial for numerous applications and provides further chemical versatility, with the incorporation of guest species such as wavelength shifters, sensitizing species, and other species that can improve the scintillation and direct detection properties of the subsequent MOFs. One notable example is the development of halide perovskite@MOF composites, which have been demonstrated to efficiently stabilize halide perovskites from environmental factors. The development of halide perovskite@MOF composites was first demonstrated in 2015, by incorporating MOF-525

nanocrystals into perovskite precursor solutions. Since then, numerous examples of halide perovskite@MOF have been shown. These composites provide an effective barrier to stabilize halide perovskites from environmental agents, and another route to sensitizing MOFs with optoelectronic properties. This provides future tunable design opportunities, harnessing the properties of multiple materials in synergistic composites. With vast possibilities for tailored synthetic designs including ligand choices and guest interactions, the chemical versatility of MOFs holds significant promise for potential applications ranging from ultrafast scintillation to high-stability direct detectors for gamma radiation.

6.2 Advanced processing techniques for scalable and uniform fabrication of MOF pixelated X-ray imaging systems.

Despite the promise of MOFs in X-ray detection, the morphology and scalability of MOFs is an important consideration for their industrial and commercial applications, including in radiation detection (see Fig. 6). Scalability can be viewed in two regards when discussing MOF X-ray detectors. The first is the scalability of MOF synthesis and manufacturing which has been thoroughly reviewed previously, highlighting the key parameters for critically evaluating the large-scale manufacturing of MOFs. The highlighted parameters include reagent and solvent costs, reaction times, reaction temperature, solvent choice, and quantity, washing, and finally processing and shaping techniques.

Some of the most common current radiation detector materials such as CsI@Tl and CZT often require long reaction times (up to 3 months), high temperature (>1000 °C), and complex growing conditions, resulting in significant costs to companies. Although in its infancy, scalable synthesis techniques of MOFs have started to grow with ongoing research into continuous MOF synthesis, mechanochemical, sonochemical and microwave assisted synthesis all providing routes to scalable low energy bulk production of MOF powders, giving promise for low-energy scalable manufacturing of MOFs for a wide variety of applications.

Our focus when discussing the scalability of MOFs for X-ray detection is on their integration into full imaging systems and

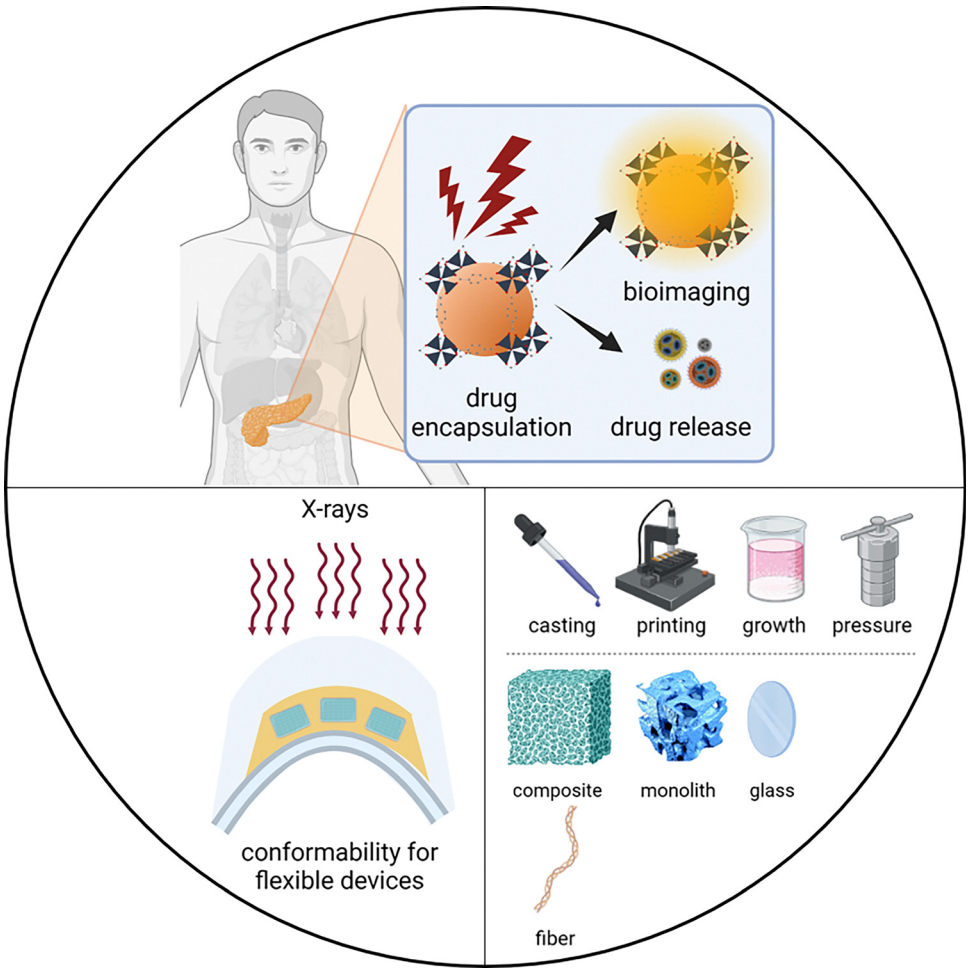

Fig. 6 Some applications and opportunities for MOF-based X-ray detectors and scintillators, and production methods. (Top) Targeted drug delivery and bioimaging using MOFs in the human body. (Bottom left) Conformability of MOFs into flexible films and devices. (Bottom right) Some fabrication methods of various MOF morphological assemblies towards scalable production. The monolith illustration was adapted with permission from ref. 29 and 91. Created with BioRender.com.

pixelated detectors. We will discuss the challenges and parameters affecting their integration and processing and shaping methods to achieve imaging systems and how this compares to alternative radiation detector materials. MOFs are typically synthesised in powder morphologies which results in some inherent limitations for MOF X-ray detectors. These include poor handling, low packing densities and poor optical quality, and inefficient charge transport. One benefit of MOF powder morphologies however can be the ease of manufacturing large scale films through pelletisation. Pelletisation of MOFs is a commonly used technique, resulting in easily shaped, and thickness-controlled pellets depending on the mould of choice.

Although impractical for scintillators due to optical transparency for visible photons to escape, pelletisation could be envisioned for pixelated direct X-ray detectors. Pixelation can be envisioned through a variety of method including incorporating a pixelated design into pelletisation moulds which would provide a low-energy and easy process to design and manufacture pelletised MOF flat panel detectors. Typical industrial pixelation techniques including roll-to-roll printing and sputtering could also be envisioned prior to flip-chip bonding onto readout electronics, although specific care and optimisation would be required to ensure pellet uniformity and low surface roughness.

Other post processing techniques of MOF powders have also been demonstrated for both scintillators and direct detectors. This includes the infiltration of mixed matrix membranes, polymer membranes with MOF powders. This process has several advantages and limitations depending on the intended applications. Membrane infiltration provides a viable pathway to create large area films, with improved optical transparency compared to raw powder MOFs. They also provide unique opportunities such as biocompatible and flexible, wearable radiation monitors. However, for applications which require high-resolution imaging, MOF doped films have limitations due to optical refraction and an uneven distribution of MOF particles.

Advanced processing techniques such as liquid phase sintering and monolithic MOF synthesis offer two processing routes which could overcome these limitations. Liquid phase sintering has been demonstrated as a scalable method to convert powdered MOFs into glassy MOFs with high optical transparency. This overcomes handling problems and the challenges with uneven distribution of MOF particles in polymer membranes, whilst maintaining their ability to encapsulate guest species. This produces robust, shape adjustable MOF glasses and composites, with potential to tune the X-ray attenuation of MOFs to specific radiation energies. This makes MOF glasses excellent candidates for both scintillator and direct radiation detectors. Pixelation of MOF glasses could be achieved *via* typical electrode processing techniques such as spin coating, thermal evaporation, sputtering or lithography with conditions dependent on the MOF of choice.

The developments in sol–gel MOF processing which have enabled the development of high-density polycrystalline MOF structures through advanced synthesis and densification, resulting in size-controllable materials could also be highly beneficial for developing MOF X-ray imaging systems. These cm-sized, monolithic MOFs exhibit superior mechanical properties, including increased hardness and Young's modulus compared to their powder, pellet, or single crystal counterparts.[27,28] Additionally, monolithic MOFs maintain, and in some cases enhance their characteristic porosity, high bulk densities, and exceptional volumetric adsorption capacities, whilst maintaining their crystalline structure, providing potential to incorporate guest species improving optoelectronic performance whilst maintaining processability. The sol–gel synthesis approach for developing scintillators was demonstrated successfully by Avila *et al.* who prepared a proof-of-concept monolithic MOF scintillator by incorporating $MAPbBr_3$ nanocrystals into the mesoporosity of the MOF ZIF-8.[92] These perovskite@MOF monoliths were developed using scalable processes, with no external pressure or heating required to form dense robust structures, with comparable optical quality of MOF glasses. This sol–gel processing technique and the use of mild drying solvents such as ethanol or water, mean monolithic MOFs could provide a future route to efficient direct growth onto commercial pixelated detectors for both scintillator and direct detector X-ray imaging systems.

6.3 Host–guest interactions and emerging biomedical applications

As mentioned previously, MOFs' permanent porosity enables the incorporation of guests within MOFs, providing opportunities for sensitisation and multifunctionality (see Fig. 6). The possibility of host–guest interactions and encapsulation enables the exploration of future applications. MOFs are favourable for biomedical applications, including cancer therapy, bioimaging and drug delivery, due to their low cytotoxicity, biodegradability arising from easily broken metal–ligand bonds, and high porosity.[93,94] Although the components that make up a MOF can be toxic separately, they can become non-toxic when merged to form a MOF.[95,96] BioMOFs, which are MOFs with at least one biomolecule (like amino acids, proteins, polypeptides, *etc.*) as a linker, have also emerged as a new subclass of MOFs.[97,98] Multifunctional theragnostic systems can be realised by loading therapeutic agents into the internal cavity of MOFs.[34] For example, a nanoscale MOF was used to co-deliver multiple therapeutics for effective medical treatment,[99] and a MOF active targeted drug delivery nanocarrier platform was designed that is also able to facilitate *in vivo* imaging with good biocompatibility and low cytotoxicity.[100] Della Rocca *et al.* summarised different strategies developed to incorporate both imaging and therapeutic agents into nanoscale MOFs, by exploiting their tunability to realise high agent loadings.[101] There is great potential for theragnostic imaging, where bioimaging is combined with drug delivery in a single ensemble, using biologically safe MOFs. Perego *et al.* noted that the material composition of MOFs can be tailored, *via* the accessible pores, to allow interactions with different types of radiation by including different elements and compounds.[41] This gives rise to the promise of multi-modal imaging[102–105] and multi-colour detection,[106] with future exciting possibilities, by sensitising MOFs in multiple ways.

MOFs which exhibit a long afterglow/persistent radioluminescence, also present great potential for *in vivo* bioimaging. For example, prolonged scintillation in the red can facilitate their detection through the skin. A common strategy for their synthesis is to dope additional ions (for example, rare earth ions) to provide the desired luminescence colours and lifetimes. Yuan *et al.* summarised a list of reported MOFs with long afterglow behaviour, and the various synthetic approaches.[107] Yan *et al.*, for instance, developed Zn-terephthalate MOFs which exhibit an afterglow emission as long as 0.47 s, which is three orders of magnitude longer than typical photoemission lifetimes in the order of hundreds of microseconds to few milliseconds in MOFs containing noble metals and rare earth metals.[108] Zhang *et al.* presented another example of a Ca-MOF with long afterglow up to 4 s and visible by the naked eye.[109]

6.4 Improved mechanical properties for durable and flexible detectors

Desired mechanical properties, such as compactness and flexibility, can be incorporated into the fabrication of MOF-based detectors, *via* polymerization procedures (see Fig. 6).[41] Wang *et al.* presented, for the first time, an X-ray detector with mechanical flexibility, prepared by a thermoplastic dispersal of MOFs with readily available polymers, where the photocurrent remained stable despite the device undergoing 500 bend cycles.[45] This work showcases the promise of MOF-based X-ray detectors for medical and industrial imaging and testing, in the form of non-planar device configurations.

Most recently, a porous hafnium-based MOF containing dicarboxy-9,10-diphenylanthracene as a scintillating conjugated ligand to detect radioactive noble gases was demonstrated for the first time.[61] The prototype detector was able to detect krypton-85 with sensitivity superior to the commercial plastic scintillator EJ-276, with the additional advantages of being more compact, cheaper, and requiring much shorter acquisition times. This work showcases the potential of radioactive gas detectors based on porous MOF crystals as scintillators to outperform existing technologies.

6.5 Advancing environmental sustainability in MOF-based detectors

Sustainability has become an increasingly important consideration in the development of X-ray detection materials, particularly for medical and industrial applications. MOFs can allow environmentally-friendly designs due to their modular and highly tunable structures. For example, Ren *et al.* demonstrated high-performance yet environmentally friendly X-ray detectors, in particular Pb-free Cu-DABDT-MOFs-based[78] and Ni-DABDT-MOFs-based[69] X-ray detectors, which show the potential for MOF detectors to reduce the reliance on hazardous and toxic materials like lead, cadmium, and mercury, otherwise commonly used in conventional detectors.

Environmentally-sustainable synthesis techniques can further enhance the appeal of MOFs. For example, electrochemical synthesis has been successfully applied to MOFs like HKUST-1 and MIL-100, using benign solvents (*e.g.*, water or ethanol) and avoiding high-energy processes.[110] New mechanochemical methods could further eliminate the need for solvents completely, reducing waste generation and energy consumption, and offering scalable routes to producing MOFs with minimal environmental consequence. These approaches, alongside typical solvothermal MOF synthesis, offer significant energy savings, compared to the long and high-temperature methods for current detector materials such as CZT and CsI:Tl. The combination of green synthesis techniques and large chemical versatility of MOF-based detectors provides a pathway to significantly reduce the environmental footprint of radiation detection technologies, which could pave the way for sustainable medical diagnostics and imaging systems.

7. Conclusion

In this review, we have covered the fundamental mechanisms, figures of merit, and recent research progress made in MOF-based detectors and scintillators for a new generation of X-ray technologies, as well as their future promise. Proofs-of-concept in research laboratories have shown that MOF-based X-ray detectors can be competitive against commercially available technologies for a range of applications including biomedical imaging and optoelectronics, with potential advantages including lower toxicity, facile synthesis, scalable production, higher performance and efficiency, environmental and irradiation stability, lower costs and durability.[77,92,111] Future research efforts will further push their sensitivity beyond current limits, enhancing imaging resolutions and reducing radiation exposure for patients. Their multi-functionality enables important applications in bioimaging, monitoring and drug delivery, among others. The development of cost-effective production techniques will also help meet the rising demand for imaging, widening access to critical healthcare and security needs for societies.

Conflicts of interest

M. A. and H. S. are co-founders of Clarity Sensors. For the purpose of open access, the authors have applied a Creative Commons Attribution (CC BY) licence to any Author Accepted Manuscript version arising from this submission.

Data availability

No primary research results, software or code have been included and no new data were generated or analysed as part of this review.

Acknowledgements

H. S. thanks the UK Engineering and Physical Sciences Research Council (EPSRC) grant EP/S023046/1 for the EPSRC Centre for Doctoral Training in Sensor Technologies for a Healthy and Sustainable Future. X. W. C. thanks the Agency

for Science, Technology and Research (A*STAR, Singapore) for the National Science Scholarship. M. A. acknowledges support by the Royal Academy of Engineering under the Research Fellowship programme and by the BBVA Foundation for their support through a Leonardo Fellowship. M. A. also acknowledges support from RYC2021-034941-I and PID2022-142525OA-I00 funded by MICIU/AEI/10.13039/501100011033, the European Union ''NextGenerationEU''/PRTR and FEDER, EU. Fig. 6 was created with the help of BioRender software.

References

1 W. C. Röntgen, *Science*, 1896, **3**, 227–231.
2 M. Nikl, *Meas. Sci. Technol.*, 2006, **17**, R37–R54.
3 Patient dose information, **https://www.gov.uk/government/publications/medical-radiation-patient-doses/patient-dose-information-guidance**, (accessed 31 March 2021).
4 E. E. Ovechkina, V. Gaysinskiy, S. R. Miller, C. Brecher, A. Lempicki and V. V. Nagarkar, *Radiat. Meas.*, 2007, **42**, 541–544.
5 J. H. Siewerdsen and D. A. Jaffray, *Med. Phys.*, 1999, **26**, 1624–1641.
6 P. A. Rodnyi, Physical Processes in Inorganic Scintillators, **https://cds.cern.ch/record/627937**, (accessed 4 January 2021).
7 Y. C. Kim, K. H. Kim, D.-Y. Son, D.-N. Jeong, J.-Y. Seo, Y. S. Choi, I. T. Han, S. Y. Lee and N.-G. Park, *Nature*, 2017, **550**, 87–91.
8 Y. Su, W. Ma and Y. (Michael) Yang, *J. Semicond.*, 2020, **41**, 051204.
9 S. R. Batten, N. R. Champness, X.-M. Chen, J. Garcia-Martinez, S. Kitagawa, L. Öhrström, M. O'Keeffe, M. P. Suh and J. Reedijk, *CrystEngComm*, 2012, **14**, 3001–3004.
10 P. Z. Moghadam, A. Li, S. B. Wiggin, A. Tao, A. G. P. Maloney, P. A. Wood, S. C. Ward and D. Fairen-Jimenez, *Chem. Mater.*, 2017, **29**, 2618–2625.
11 P. Z. Moghadam, A. Li, X.-W. Liu, R. Bueno-Perez, S.-D. Wang, S. B. Wiggin, P. A. Wood and D. Fairen-Jimenez, *Chem. Sci.*, 2020, **11**, 8373–8387.
12 P. Z. Moghadam, T. Islamoglu, S. Goswami, J. Exley, M. Fantham, C. F. Kaminski, R. Q. Snurr, O. K. Farha and D. Fairen-Jimenez, *Nat. Commun.*, 2018, **9**, 1378.
13 G. E. Gomez and F. Roncaroli, *Inorg. Chim. Acta*, 2020, **513**, 119926.
14 C. Li, L. Zhang, J. Chen, X. Li, J. Sun, J. Zhu, X. Wang and Y. Fu, *Nanoscale*, 2021, **13**, 485–509.
15 Y. Zhou, J. Chen, O. M. Bakr and O. F. Mohammed, *ACS Energy Lett.*, 2021, 739–768.
16 R. H. Pratt, A. Ron and H. K. Tseng, *Rev. Mod. Phys.*, 1973, **45**, 273–325.
17 J. B. A. England, *J. Phys.*, 1976, **9**, 233–251.
18 H. Wei and J. Huang, *Nat. Commun.*, 2019, **10**, 1066.
19 *Radiation oncology physics: a handbook for teachers and students*, ed. E. B. Podgorsak, International Atomic Energy Agency Publication, 2005.
20 A. Jana, S. Cho, S. A. Patil, A. Meena, Y. Jo, V. G. Sree, Y. Park, H. Kim, H. Im and R. A. Taylor, *Mater. Today*, 2022, **55**, 110–136.
21 M. Spahn, *Nucl. Instrum. Methods Phys. Res., Sect. A*, 2013, **731**, 57–63.
22 G. F. Knoll, *Radiation detection and measurement*, Wiley, New York, 3rd edn, 2000.
23 NIST XCOM: Photon Cross Sections Database - Version History, **https://physics.nist.gov/PhysRefData/Xcom/Text/version.shtml**, (accessed 20 January 2023).
24 A. Li, R. B. Perez, S. Wiggin, S. C. Ward, P. A. Wood and D. Fairen-Jimenez, *Matter*, 2021, **4**, 1105–1106.
25 J. Lu, X.-H. Xin, Y.-J. Lin, S.-H. Wang, J.-G. Xu, F.-K. Zheng and G.-C. Guo, *Dalton Trans.*, 2019, **48**, 1722–1731.
26 D. F. Jackson and D. J. Hawkes, *Phys. Rep.*, 1981, **70**, 169–233.
27 T. Tian, Z. Zeng, D. Vulpe, M. E. Casco, G. Divitini, P. A. Midgley, J. Silvestre-Albero, J.-C. Tan, P. Z. Moghadam and D. Fairen-Jimenez, *Nat. Mater.*, 2018, **17**, 174–179.
28 T. Tian, J. Velazquez-Garcia, T. D. Bennett and D. Fairen-Jimenez, *J. Mater. Chem. A*, 2015, **3**, 2999–3005.
29 J. Hou, A. F. Sapnik and T. D. Bennett, *Chem. Sci.*, 2020, **11**, 310–323.
30 A. G. Al Lafi, B. Assfour and T. Assaad, *J. Mater. Sci.*, 2021, **56**, 12154–12170.
31 S. E. Gilson, M. Fairley, P. Julien, A. G. Oliver, S. L. Hanna, G. Arntz, O. K. Farha, J. A. LaVerne and P. C. Burns, *J. Am. Chem. Soc.*, 2020, **142**, 13299–13304.
32 C. Volkringer, C. Falaise, P. Devaux, R. Giovine, V. Stevenson, F. Pourpoint, O. Lafon, M. Osmond, C. Jeanjacques, B. Marcillaud, J. C. Sabroux and T. Loiseau, *Chem. Commun.*, 2016, **52**, 12502–12505.
33 S. L. Hanna, D. X. Rademacher, D. J. Hanson, T. Islamoglu, A. K. Olszewski, T. M. Nenoff and O. K. Farha, *Ind. Eng. Chem. Res.*, 2020, **59**, 7520–7526.
34 C. Wang, O. Volotskova, K. Lu, M. Ahmad, C. Sun, L. Xing and W. Lin, *J. Am. Chem. Soc.*, 2014, **136**, 6171–6174.
35 K. E. deKrafft, W. S. Boyle, L. M. Burk, O. Z. Zhou and W. Lin, *J. Mater. Chem.*, 2012, **22**, 18139–18144.
36 M. Koshimizu, *Jpn. J. Appl. Phys.*, 2022, **62**, 010503.
37 T. A. King, R. Voltz and B. H. Flowers, *Proc. R. Soc. London, Ser. A*, 1997, **289**, 424–439.
38 S. R. Mathis, S. T. Golafale, K. M. Solntsev and C. W. Ingram, *Crystals*, 2018, **8**, 53.
39 W. Zhu, H. Yu, X. Zhu and H. Li, *Inorg. Chem. Commun.*, 2022, **136**, 109182.
40 Y. Wang, X. Yin, W. Liu, J. Xie, J. Chen, M. A. Silver, D. Sheng, L. Chen, J. Diwu, N. Liu, Z. Chai, T. E. Albrecht-Schmitt and S. Wang, *Angew. Chem., Int. Ed.*, 2018, **57**, 7883–7887.
41 J. Perego, I. Villa, A. Pedrini, E. C. Padovani, R. Crapanzano, A. Vedda, C. Dujardin, C. X. Bezuidenhout, S. Bracco, P. E. Sozzani, A. Comotti, L. Gironi, M. Beretta, M. Salomoni, N. Kratochwil, S. Gundacker, E. Auffray, F. Meinardi and A. Monguzzi, *Nat. Photonics*, 2021, **15**, 393–400.

42 Y. Zhang, X. Wang, K. Xu, F. Zhai, J. Shu, Y. Tao, J. Wang, L. Jiang, L. Yang, Y. Wang, W. Liu, J. Su, Z. Chai and S. Wang, *J. Am. Chem. Soc.*, 2023, **145**, 13161–13168.
43 X. Liu, R. Li, X. Xu, Y. Jiang, W. Zhu, Y. Yao, F. Li, X. Tao, S. Liu, W. Huang and Q. Zhao, *Adv. Mater.*, 2023, **35**, 2206741.
44 Q. Chen, J. Wu, X. Ou, B. Huang, J. Almutlaq, A. A. Zhumekenov, X. Guan, S. Han, L. Liang, Z. Yi, J. Li, X. Xie, Y. Wang, Y. Li, D. Fan, D. B. L. Teh, A. H. All, O. F. Mohammed, O. M. Bakr, T. Wu, M. Bettinelli, H. Yang, W. Huang and X. Liu, *Nature*, 2018, **561**, 88–93.
45 C. Liang, S. Zhang, L. Cheng, J. Xie, F. Zhai, Y. He, Y. Wang, Z. Chai and S. Wang, *Angew. Chem., Int. Ed.*, 2020, **59**, 11856–11860.
46 Q. Hu, Z. Deng, M. Hu, A. Zhao, Y. Zhang, Z. Tan, G. Niu, H. Wu and J. Tang, *Sci. China: Chem.*, 2018, **61**, 1581–1586.
47 F. Yang, A. Wang, S. Yue, W. Du, S. Wang, X. Zhang and X. Liu, *Sci. China Mater.*, 2021, **64**, 2889–2914.
48 B. Yang, L. Yin, G. Niu, J.-H. Yuan, K.-H. Xue, Z. Tan, X.-S. Miao, M. Niu, X. Du, H. Song, E. Lifshitz and J. Tang, *Adv. Mater.*, 2019, **31**, 1904711.
49 J. Gao, J. Lu, B. Li, W. Wang, M. Xie, S. Wang, F. Zheng and G. Guo, *Chin. Chem. Lett.*, 2022, **33**, 5132–5136.
50 J.-X. Wang, L. Gutiérrez-Arzaluz, X. Wang, M. Almalki, J. Yin, J. Czaban-Jóźwiak, O. Shekhah, Y. Zhang, O. M. Bakr, M. Eddaoudi and O. F. Mohammed, *Matter*, 2022, **5**, 253–265.
51 W.-F. Wang, J. Lu, X.-M. Xu, B.-Y. Li, J. Gao, M.-J. Xie, S.-H. Wang, F.-K. Zheng and G.-C. Guo, *Chem. Eng. J.*, 2022, **430**, 133010.
52 J. Perego, C. X. Bezuidenhout, I. Villa, F. Cova, R. Crapanzano, I. Frank, F. Pagano, N. Kratochwill, E. Auffray, S. Bracco, A. Vedda, C. Dujardin, P. E. Sozzani, F. Meinardi, A. Comotti and A. Monguzzi, *Nat. Commun.*, 2022, **13**, 3504.
53 M.-J. Xie, W.-F. Wang, B.-Y. Li, J. Gao, Y.-F. Yan, J. Lu, F.-K. Zheng and G.-C. Guo, *Inorg. Chem. Commun.*, 2022, **142**, 109711.
54 C. Dujardin, E. Auffray, E. Bourret-Courchesne, P. Dorenbos, P. Lecoq, M. Nikl, A. N. Vasil'ev, A. Yoshikawa and R.-Y. Zhu, *IEEE Trans. Nucl. Sci.*, 2018, **65**, 1977–1997.
55 F. Maddalena, L. Tjahjana, A. Xie, Arramel, S. Zeng, H. Wang, P. Coquet, W. Drozdowski, C. Dujardin, C. Dang and M. D. Birowosuto, *Crystals*, 2019, **9**, 88.
56 Q.-C. Peng, Y.-B. Si, J.-W. Yuan, Q. Yang, Z.-Y. Gao, Y.-Y. Liu, Z.-Y. Wang, K. Li, S.-Q. Zang and B. Zhong Tang, *Angew. Chem., Int. Ed.*, 2023, **62**, e202308194.
57 P. L. Feng, J. V. Branson, K. Hattar, G. Vizkelethy, M. D. Allendorf and F. Patrick Doty, *Nucl. Instrum. Methods Phys. Res., Sect. A*, 2011, **652**, 295–298.
58 R. M. Turtos, S. Gundacker, E. Auffray and P. Lecoq, *Phys. Med. Biol.*, 2019, **64**, 185018.
59 Z. Meng, F. Chen, P. Shen, L. Lei, H. Xu and S. Xu, *J. Solid State Chem.*, 2024, **329**, 124425.
60 O. D. I. Moseley, T. Doherty, R. Parmee, M. Anaya and S. D. Stranks, *J. Mater. Chem. C*, 2019, **9**, 11588–11604.
61 M. Orfano, J. Perego, F. Cova, C. X. Bezuidenhout, S. Piva, C. Dujardin, B. Sabot, S. Pierre, P. Mai, C. Daniel, S. Bracco, A. Vedda, A. Comotti and A. Monguzzi, *Nat. Photonics*, 2023, **17**, 672–678.
62 Y. Wu, J. Feng, Z. Yang, Y. Liu and S. (Frank) Liu, *Adv. Sci.*, 2023, **10**, 2205536.
63 M. Overdick, C. Baumer, K. J. Engel, J. Fink, C. Herrmann, H. Kruger, M. Simon, R. Steadman and G. Zeitler, *IEEE Trans. Nucl. Sci.*, 2009, **56**, 1800–1809.
64 S. Kasap, J. B. Frey, G. Belev, O. Tousignant, H. Mani, L. Laperriere, A. Reznik and J. A. Rowlands, *Phys. Status Solidi B*, 2009, **246**, 1794–1805.
65 S. Tokuda, H. Kishihara, S. Adachi and T. Sato, *J. Mater. Sci.: Mater. Electron.*, 2004, **15**, 1–8.
66 S. Del Sordo, L. Abbene, E. Caroli, A. M. Mancini, A. Zappettini and P. Ubertini, *Sensors*, 2009, **9**, 3491–3526.
67 X.-Y. Yu, J.-R. Mi, Q.-P. Qin, X.-P. Fang, Y.-F. Han, L.-Z. Cai, M.-S. Wang and G.-C. Guo, *Inorg. Chem. Front.*, 2024, **11**, 3316–3322.
68 Y.-F. Han, X.-M. Xu, S.-H. Wang, W.-F. Wang, M.-S. Wang and G.-C. Guo, *Chem. Eng. J.*, 2022, **437**, 135468.
69 Z. Li, S. Chang, H. Zhang, Y. Hu, Y. Huang, L. Au and S. Ren, *Nano Lett.*, 2021, **21**, 6983–6989.
70 Q. Wei, J. Liu, L. Wu, F. Chen, Y. Ye, S. Zhang, Y. Zhu, Y. Chen, M. You, Q. Liao, M. Lin and H. Chen, *Small*, 2024, **20**, 2405932.
71 H. Mescher, E. Hamann and U. Lemmer, *Sci. Rep.*, 2019, **9**, 5231.
72 L. Basiricò, A. Ciavatti and B. Fraboni, *Adv. Mater. Technol.*, 2021, **6**, 2000475.
73 H. Mescher, F. Schackmar, H. Eggers, T. Abzieher, M. Zuber, E. Hamann, T. Baumbach, B. S. Richards, G. Hernandez-Sosa, U. W. Paetzold and U. Lemmer, *ACS Appl. Mater. Interfaces*, 2020, **12**, 15774–15784.
74 S. Kasap, J. B. Frey, G. Belev, O. Tousignant, H. Mani, J. Greenspan, L. Laperriere, O. Bubon, A. Reznik, G. DeCrescenzo, K. S. Karim and J. A. Rowlands, *Sensors*, 2011, **11**, 5112–5157.
75 C. A. Klein, *J. Appl. Phys.*, 1968, **39**, 2029–2038.
76 R. C. Alig and S. Bloom, *Phys. Rev. Lett.*, 1975, **35**, 1522–1525.
77 C. Liang, L. Cheng, S. Zhang, S. Yang, W. Liu, J. Xie, M.-D. Li, Z. Chai, Y. Wang and S. Wang, *J. Am. Chem. Soc.*, 2022, **144**, 2189–2196.
78 Z. Li, S. Chang, H. Zhang, Y. Hu, Y. Huang, L. An and S. Ren, *Chem. Commun.*, 2021, **57**, 8612–8615.
79 Y. Wang, X. Liu, X. Li, F. Zhai, S. Yan, N. Liu, Z. Chai, Y. Xu, X. Ouyang and S. Wang, *J. Am. Chem. Soc.*, 2019, **141**, 8030–8034.
80 L. Cheng, C. Liang, B. Li, H. Qin, P. Mi, B. Chen, Y. Yan, X. Dai, C. Zhang, Y. Wang, Y. Wang and S. Wang, *Cell Rep. Phys. Sci.*, 2022, **3**, 101004.
81 M. Xu, J. Liu, W. Wu, Y. Chen, D. Ma, S. Chen, W. Jie, M. Zhu and Y. Xu, *Nano Res.*, 2024, **17**, 2988–2993.
82 K. Kim, S. Ahn, S. An, J. Hong, Y. Yi and S. Kim, *Curr. Appl. Phys.*, 2007, **7**, 296–299.
83 C. Szeles, *Phys. Status Solidi B*, 2004, **241**, 783–790.
84 H. Du, L. E. Antonuk, Y. El-Mohri, Q. Zhao, Z. Su, J. Yamamoto and Y. Wang, *Phys. Med. Biol.*, 2008, **53**, 1325.

85 K. M. Oh, D. K. kim, J. W. Shin, S. U. Heo, J. S. Kim, J. G. Park and S. H. Nam, *J. Instrum.*, 2014, **9**, P01010.
86 W. Pan, H. Wu, J. Luo, Z. Deng, C. Ge, C. Chen, X. Jiang, W.-J. Yin, G. Niu, L. Zhu, L. Yin, Y. Zhou, Q. Xie, X. Ke, M. Sui and J. Tang, *Nat. Photonics*, 2017, **11**, 726–732.
87 S. Shrestha, R. Fischer, G. J. Matt, P. Feldner, T. Michel, A. Osvet, I. Levchuk, B. Merle, S. Golkar, H. Chen, S. F. Tedde, O. Schmidt, R. Hock, M. Rührig, M. Göken, W. Heiss, G. Anton and C. J. Brabec, *Nat. Photonics*, 2017, **11**, 436–440.
88 J. D. Valentine, W. W. Moses, S. E. Derenzo, D. K. Wehe and G. F. Knoll, *Nucl. Instrum. Methods Phys. Res., Sect. A*, 1993, **325**, 147–157.
89 C. Michail, V. Koukou, N. Martini, G. Saatsakis, N. Kalyvas, A. Bakas, I. Kandarakis, G. Fountos, G. Panayiotakis and I. Valais, *Crystals*, 2020, **10**, 429.
90 C. L. Melcher and J. S. Schweitzer, *IEEE Trans. Nucl. Sci.*, 1992, **39**, 502–505.
91 N. Moitra, S. Fukumoto, J. Reboul, K. Sumida, Y. Zhu, K. Nakanishi, S. Furukawa, S. Kitagawa and K. Kanamori, *Chem. Commun.*, 2015, **51**, 3511–3514.
92 E. Avila, H. Salway, E. Ruggeri, C. Çamur, N. Rampal, T. A. S. Doherty, O. D. I. Moseley, S. D. Stranks, D. Fairen-Jimenez and M. Anaya, *Matter*, 2024, 7(12), 4319–4331.
93 J. Munawar, M. S. Khan, S. E. Zehra Syeda, S. Nawaz, F. A. Janjhi, H. Ul Haq, E. U. Rashid, T. Jesionowski and M. Bilal, *Inorg. Chem. Commun.*, 2023, **147**, 110145.
94 D. De and P. Sahoo, *Dalton Trans.*, 2022, **51**, 9950–9965.
95 C. Tamames-Tabar, D. Cunha, E. Imbuluzqueta, F. Ragon, C. Serre, M. J. Blanco-Prieto and P. Horcajada, *J. Mater. Chem. B*, 2013, **2**, 262–271.
96 D.-Y. Fu, X. Liu, X. Zheng, M. Zhou, W. Wang, G. Su, T. Liu, L. Wang and Z. Xie, *Coord. Chem. Rev.*, 2022, **456**, 214393.
97 I. Imaz, M. Rubio-Martínez, J. An, I. Solé-Font, N. L. Rosi and D. Maspoch, *Chem. Commun.*, 2011, **47**, 7287–7302.
98 G. Awasthi, S. Shivgotra, S. Nikhar, S. Sundarrajan, S. Ramakrishna and P. Kumar, *Polymers*, 2022, **14**, 4710.
99 C. He, K. Lu, D. Liu and W. Lin, *J. Am. Chem. Soc.*, 2014, **136**, 5181–5184.
100 Q. Zhang, J. Li, W. Zu, H. Yang and Y. Wang, *Drug Dev. Ind. Pharm.*, 2021, **47**, 1175–1182.
101 J. Della Rocca, D. Liu and W. Lin, *Acc. Chem. Res.*, 2011, **44**, 957–968.
102 X. Lai, H. Jiang and X. Wang, *Biosensors*, 2021, **11**, 299.
103 Z. Zhang, W. Sang, L. Xie and Y. Dai, *Coord. Chem. Rev.*, 2019, **399**, 213022.
104 B. Ling, Y. Wang, R. Mi, D. Wang, H. Chen, X. Li, Y. Zhang and L. Wang, *Chem. – Asian J.*, 2022, **17**, e202200161.
105 W. Cai, H. Gao, C. Chu, X. Wang, J. Wang, P. Zhang, G. Lin, W. Li, G. Liu and X. Chen, *ACS Appl. Mater. Interfaces*, 2017, **9**, 2040–2051.
106 S. Wu, C. Li, H. Shi, Y. Huang and G. Li, *Anal. Chem.*, 2018, **90**, 9929–9935.
107 J. Yuan, J. Dong, S. Lei and W. Hu, *Mater. Chem. Front.*, 2021, **5**, 6824–6849.
108 X. Yang and D. Yan, *Chem. Sci.*, 2016, **7**, 4519–4526.
109 D.-F. Lu, Y. Sun, Z.-Y. Ye, C.-C. Feng, F. Wang and J. Zhang, *ACS Omega*, 2022, **7**, 22015–22019.
110 Y. Liu, T. Jiang and Z. Liu, *Nanotheranostics*, 2022, **6**, 143–160.
111 H. Chen, J. Chen, M. Li, M. You, Q. Chen, M. Lin and H. Yang, *Sci. China: Chem.*, 2022, **65**, 2338–2350.

